WARSAW UNIVERSITY OF TECHNOLOGY

DISCIPLINE OF SCIENCE - CHEMICAL ENGINEERING/

FIELD OF SCIENCE - ENGINEERING AND TECHNOLOGY

Ph.D. Thesis

Krystian Jędrzejczak, M.Sc.

Diagnostics of hemolysis risk in atherosclerosis - numerical analysis and experimental studies

Supervisor

Łukasz Makowski, Prof., Ph.D., D.Sc.

Co-supervisor

Wojciech Orciuch, Ph.D.

WARSAW 2024

I would like to thank my supervisors

prof. dr. hab. inż. Łukasz Makowski

and

dr inż. Wojciech Orciuch

and my colleague

mgr. inż. Arkadiusz Antonowicz

for their support during the work on my doctoral dissertation.

I would like to thank dr hab. n. med. Michał Kozłowski from Medical University of Silesia, ppłk dr n. med. Piotr Piasecki, dr n. med. Jerzy Narloch and lek. Marek Wierzbicki from Military Institute of Medicine and dr Malenka M. Bissell DPhil, MD, BM, MRCPCH, FSCMR from Leeds Institute of Cardiovascular and Metabolic Medicine for their cooperation, valuable and substantive discussions and support.

I would also like to thank my family and friends for their support.

I dedicate this work to my beloved wife Aleksandra

Table of Contents

Abstract of the Doctoral Thesis

Diagnostics of hemolysis risk in atherosclerosis - numerical analysis and experimental studies

Cardiovascular diseases are one of the leading causes of death in 21st-century society. One of the most common cardiovascular diseases is coronary artery atherosclerosis. Accumulating cholesterol causes significant narrowing of arterial vessels, which increases the risk of hemolysis due to high shear stresses acting on erythrocytes in the area of narrowed arteries.

In the course of a doctoral dissertation, a new numerical model of blood rheology was developed based on the population balance of red blood cell aggregates, which takes into account the process of mechanical hemolysis. Furthermore, based on medical imaging data, a series of 3D models of stenosed arteries were developed. These models were later used to prepare numerical meshes for CFD simulations and to develop vascular system phantoms for both PIV studies and training materials for physicians.

A series of CFD simulations have demonstrated the influence of the shape of the atherosclerotic stenosis on the maximum shear stresses, which are associated with the risk of hemolysis in the vessels. It was shown that the risk of hemolysis is highest in small vessels where sudden and significant narrowing of the artery lumen occurs. The impact of physical activity and coexisting hypertension on the increased risk of hemolysis was determined. The obtained results were validated using 3D-printed artery phantoms produced on a Form 3B+ printer, utilizing equipment for micro particle image velocimetry (μPIV). Additionally, 3D printing was used to develop a training station for angioplasty with stent implantation for training procedures for interventional radiologists and surgeons.

In summary, through a series of articles, numerical and experimental modeling of the phenomenon of hemolysis in the arteries of patients with atherosclerosis was presented, which allowed for the development of guidelines for physicians and tools for effective treatment planning to reduce the risk of perioperative complications.

Keywords: hemolysis, atherosclerosis, computational fluid dynamics, 3D printing, particle image velocimetry

Streszczenie rozprawy doktorskiej

Diagnostyka ryzyka hemolizy w miażdżycy - analiza numeryczna i badania doświadczalne

Choroby układu krwionośnego są jednym z najczęstszych powodów śmierci w społeczeństwie XXI wieku. Jedną z najczęstszych chorób układu krwionośnego jest miażdżyca tętnic wieńcowych. Gromadzący się cholesterol powoduje znaczące ograniczenie światła naczyń tętnic co powoduje wzrost ryzyka hemolizy spowodowanej wysokimi naprężeniami ścinającymi działającymi na erytrocyty w obszarze zwężonych tętnic.

W ramach pracy doktorskiej opracowano nowy model numeryczny reologii krwi w oparciu o bilans populacji aglomeratów czerwonych krwinek, który uwzględnia proces mechanicznej hemolizy. Ponadto w oparciu o dane z obrazowania medycznego opracowane szereg modeli 3D przewężonych tętnic. Uzyskane model posłużyły w dalszym etapie do przygotowania siatek numerycznym do obliczeń CFD oraz w celu opracowania modeli fantomów układu krwionośnego zarówno do badań PIV jak i jako materiały treningowe dla lekarzy.

W wyniku szeregu symulacji CFD wykazano wpływ kształtu przewężenia miażdżycowego na maksymalne naprężenia ścinające, które wiążą się z ryzykiem hemolizy w naczyniach. Wykazano, iż ryzyko hemolizy jest największe w przypadku małych naczyń w których występują nagłe i znaczące przewężenia światła tętnicy. Określono wpływ aktywności fizycznej i współistniejącego nadciśnienia tętniczego na wzrost ryzyka hemolizy. Uzyskane wyniki zostały zweryfikowane z wykorzystaniem wydrukowanych na drukarce 3D Form 3B+ fantomów tętnic korzystając z aparatury do mikro anemometrii obrazowej (μPIV). Ponadto druk 3D posłużył do opracowania modelu stanowiska do treningu angioplastyki z implantacją stentu do treningu zabiegów dla radiologów interwencyjnych i chirurgów.

Podsumowując, w ramach cyklu artykułów zaprezentowano numeryczne i eksperymentalne modelowanie zjawiska hemolizy w tętnicach u pacjentów z miażdżycą, które to pozwoliło na opracowanie wytycznych dla lekarzy oraz opracowania narzędzi do skutecznego planowania leczenia w celu ograniczenia ryzyka powikłań około operacyjnego.

Słowa kluczowe: hemoliza, miażdżyca, obliczeniowa mechanika płynów, druk 3D, anemometria obrazowa

List of publications included in the doctoral dissertation (**data from 2024)*

P1 – **Krystian Jędrzejczak,** Łukasz Makowski, Wojciech Orciuch. Model of blood rheology including hemolysis based on population balance. *Communications in Nonlinear Science and Numerical Simulation.* 2023; 116(11):106802. DOI: 10.1016/j.cnsns.2022.106802. (*IF: 3.9; CS: 7.5; ministerial points: 100)

P2 – **Krystian Jędrzejczak,** Łukasz Makowski, Wojciech Orciuch, Krzysztof Wojtas, Michał Kozłowski. Hemolysis of red blood cells in blood vessels modeled via computational fluid dynamics. *International Journal for Numerical Methods in Biomedical Engineering*. 2023; 39(11). DOI: 10.1002/cnm.3699. (*IF: 2.41; CS: 4.8; ministerial points: 100)

P3 – **Krystian Jędrzejczak,** Arkadiusz Antonowicz, Łukasz Makowski, Wojciech Orciuch, Krzysztof Wojtas, Michał Kozłowski. Computational fluid dynamics validated by micro particle image velocimetry to estimate the risk of hemolysis in arteries with atherosclerotic lesions. *Chemical Engineering Research and Design.* 2023; 196:342-353. DOI: 10.1016/j.cherd.2023.06.041. (*IF: 3.9; CS: 6.5; ministerial points: 140)

P4 – **Krystian Jędrzejczak,** Wojciech Orciuch, Krzysztof Wojtas, Michał Kozłowski, Piotr Piasecki, Jerzy Narloch, Marek Wierzbicki, Łukasz Makowski. Prediction of Hemodynamic-Related Hemolysis in Carotid Stenosis and Aiding in Treatment Planning and Risk Stratification Using Computational Fluid Dynamics. *Biomedicines.* 2024; 12(1):37. DOI: 10.3390/biomedicines12010037. (*IF: 4.7; CS: 3.7; ministerial points: 100)

P5 – **Krystian Jędrzejczak,** Arkadiusz Antonowicz, Beata Butruk-Raszeja, Wojciech Orciuch, Krzysztof Wojtas, Piotr Piasecki, Jerzy Narloch, Marek Wierzbicki Łukasz Makowski. Three-Dimensionally Printed Elastic Cardiovascular Phantoms for Carotid Angioplasty Training and Personalized Healthcare. *Journal of Clinical Medicine.* 2024; 13(17):5115. DOI: 10.3390/jcm13175115. (*IF: 3.0; CS: 5.7; ministerial points: 140)

P6 – **Krystian Jędrzejczak,** Wojciech Orciuch, Krzysztof Wojtas, Piotr Piasecki, Jerzy Narloch, Marek Wierzbicki, Michał Kozłowski, Malenka Bissell, Łukasz Makowski. Impact of Hypertension and Physical Exercise on Hemolysis Risk in the Left Coronary Artery: A CFD Analysis. *Journal of Clinical Medicine.* 2024; 13(20):6163. DOI: 10.3390/jcm13206163. (*IF: 3.0; CS: 5.7; ministerial points: 140)

Author's contribution to specific papers

P1 – First author – conceptualization, methodology, software, validation, formal analysis, investigation, resources, data curation, writing – original draft, visualization.

P2 – First author – conceptualization, methodology, software, validation, formal analysis, investigation, resources, data curation, writing – original draft, visualization.

P3 – First author – conceptualization, methodology, software, validation, formal analysis, investigation, resources, data curation, writing – original draft, visualization.

P4 – First author – conceptualization, methodology, validation, investigation, resources, data curation, writing—original draft preparation, writing—review and editing, visualization, funding acquisition.

P5 – First author — conceptualization, methodology, software, validation, formal analysis, investigation, resources, data curation, writing—original draft preparation, visualization, funding acquisition.

P6 – First author — conceptualization, methodology, software, validation, formal analysis, investigation, resources, data curation, writing—original draft preparation, visualization, funding acquisition.

Detailed author contributions to each article are presented before each article at the end of the thesis.

List of projects and research internship that research has been included in the dissertation

Zastosowanie obliczeniowej mechaniki płynów oraz laserowych metod pomiarowych przepływu w analizie mechanizmów hemolizy i defektów czynnika von Willebranda występujących w przeciekach wokół sztucznych zastawek mitralnych

[Application of computational fluid dynamics and laser flow measurement methods in the analysis of hemolysis mechanisms and von Willebrand factor defects occurring in perivalvular leaks around artificial mitral valves.]

BIOTECHMED-1, Excellence Initiative – Research University, 2020

Metody szacowania ryzyka pierwotnego i wtórnego zarastania tętnic towarzyszącego chorobie wieńcowej z zastosowaniem obliczeniowej mechaniki płynów, technik obrazowych pomiaru przepływu oraz druku 3D

[Methods for estimating the risk of primary and secondary arterial restenosis associated with coronary artery disease using computational fluid dynamics, flow imaging techniques, and 3D printing.]

BIOTECHMED-3, Excellence Initiative – Research University, 2021

Analiza zjawiska hemolizy występującej w bifurkacjach w przypadku schorzeń lewej i prawej tętnicy wieńcowej – badania doświadczalne oraz modelowanie teoretyczne.

[Analysis of hemolysis occurring in bifurcations in left and right coronary artery diseases – experimental studies and theoretical modeling.]

YOUNG PW, Excellence Initiative – Research University, 2023

Staż naukowy na Uniwersytecie w Leeds, Wielka Brytania, 1. września – 29. listopada 2024

[Research internship at the University of Leeds, UK, September 1st - November 29th 2024]

Mobility PW, Excellence Initiative – Research University, 2024

Awards

1. Team Award of the 1st degree of the Rector of the Warsaw University of Technology for scientific achievements in 2022-2023.
2. Rector's Award for exceptional social activity in the 2021/2022 academic year.
3. Dean's Award for exceptional social activity in the 2022/2023 academic year.
4. Dean's Award for scientific achievements and exceptional social activity in the 2023/2024 academic year.

Conference presentations related to the topic of the doctoral dissertation

1. 9th European Young Engineers Conference, April 19-21, 2021, Warsaw, Poland, with **oral presentation** entitled "Theoretical model of blood rheology including hemolysis". **Krystian Jędrzejczak**, Łukasz Makowski, Wojciech Orciuch;
2. 10th European Young Engineers Conference, April 4-6, 2022, Warsaw, Poland, with **oral presentation** entitled "CFD simulation of blood flow through arteries with atherosclerosis". **Krystian Jędrzejczak**, Łukasz Makowski, Wojciech Orciuch;
3. X Kongres Technologii Chemicznej, May 11-14, 2022, Wrocław, Poland, with **oral presentation** entitled "Zastosowanie metodologii inżynierii chemicznej w modelowaniu schorzeń układu krwionośnego". **Krystian Jędrzejczak**, Łukasz Makowski, Wojciech Orciuch, Michał Kozłowski;
4. 7th International Conference on Computational & Mathematical Biomedical Engineering, June 27-29, 2022, Milan, Italy, with **oral presentation** entitled "Modeling hemolysis of blood in blood vessels in patients with atherosclerosis". **Krystian Jędrzejczak**, Michał Kozłowski, Łukasz Makowski, Wojciech Orciuch;
5. 7th International Conference on Computational & Mathematical Biomedical Engineering, June 27-29, 2022, Milan, Italy, with **oral presentation** entitled "PIV and CFD comparison of 3D printed blood vessels models". Arkadiusz Antonowicz, **Krystian Jędrzejczak**, Michał Kozłowski, Łukasz Makowski, Wojciech Orciuch;
6. 11th European Young Engineers Conference, April 17-19, 2023, Warsaw, Poland, with **oral presentation** entitled "Application of computational fluid dynamics to assess the risk of hemolysis in patients with atherosclerosis". **Krystian Jędrzejczak**, Łukasz Makowski, Wojciech Orciuch, Krzysztof Wojtas;
7. 24th Polish Conference of Chemical and Process Engineering, June 13-16, 2023, Warsaw, Poland, with **oral presentation** entitled "Influence of blood rheology and changes in the degree of atherosclerotic stenosis in assessing the risk of hemolysis". **Krystian Jędrzejczak**, Łukasz Makowski, Wojciech Orciuch, Krzysztof Wojtas;
8. XIV Ogólnopolska Konferencja Naukowa „Postępy Inżynierii Bioreaktorowej", September 25-27, 2023, Lodz, Poland, with **oral presentation** entitled "Zastosowanie metod inżynierii chemicznej w przewidywaniu hemolizy krwi – obliczenia numeryczne i weryfikacja doświadczalna". **Krystian Jędrzejczak**, Arkadiusz Antonowicz, Krzysztof Wojtas, Wojciech Orciuch, Łukasz Makowski;

9. XXIII Polish Conference on Biocybernetics and Biomedical Engineering, September 27-29, 2023, Lodz, Poland, with **oral presentation** entitled "Numerical simulations and experimental research of hemolysis in atherosclerosis". **Krystian Jędrzejczak**, Arkadiusz Antonowicz, Krzysztof Wojtas, Wojciech Orciuch, Michał Kozłowski, Łukasz Makowski;

10. 12th European Young Engineers Conference, April 15-17, 2024, Warsaw, Poland, with **oral presentation** entitled "Application of computational fluid dynamics to assess the risk of hemolysis in patients with atherosclerosis". **Krystian Jędrzejczak**, Łukasz Makowski, Wojciech Orciuch, Krzysztof Wojtas;

11. Chemical Engineering as Applied to Medicine 2024, May 20, 2024, Solerno, Italy, with **oral presentation** entitled "Hemolysis risk assessment in cardiovascular defects using Computational Fluid Dynamics simulations". Krzysztof Wojtas, **Krystian Jędrzejczak**, Krzysztof Truchel, Arkadiusz Antonowicz, Wojciech Orciuch, Michał Kozłowski, Piotr Piasecki, Łukasz Makowski;

12. XII Ogólnopolska Konferencja Naukowa Inżynieria Chemiczna i Procesowa dla Środowiska i Medycyny, September 11-14, 2024, Sarbinowo k/Koszalina, Poland, "Chemical engineering methodology as support in diagnostics of circulatory system diseases". **Krystian Jędrzejczak**, Krzysztof Truchel, Krzysztof Wojtas, Wojciech Orciuch, Piotr Piasecki, Mikołaj Sługocki, Bogdan Ciszek, Łukasz Makowski.

Abbreviations and formulas

Here is the list sorted alphabetically based on the first letters of each row:

- 3D – Three-dimensional
- CABG – Coronary artery bypass graft
- CFD – computational fluid dynamics
- CT – computed tomography
- DICOM – Digital Imaging and Communications in Medicine
- DQMOM – Direct Quadrature Methods of Moments
- ECMO – Extracorporeal Membrane Oxygenation
- EPIV – Echo Particle Image Velocimetry
- FDM – Fused Deposition Modeling
- Fe – iron
- FFF – Fused Filament Fabrication
- FFR – fractional flow reserve
- LAD – left anterior descending
- LCx – left circumflex
- LFS – low-force stereolitography
- LM – left main
- MRI – magnetic resonance imaging
- OSI – oscillatory shear index
- PBBR – population balance based rheology

- PBF – Powder Bed Fusion

- Pe – Pecklet number

- PIV – Particle image velocimetry

- PLAD – proximal left anterior descending coronary artery

- PLCx – proximal left circumflex

- PolyJet – Material Jetting

- QMOM – Quadrature Method of Moments

- RBC – red blood cell

- Re – Reynolds number

- RI – ramus intermedicus

- RMSE – root mean square error

- RRT – relative residence time

- SLA – stereolithography apparatus

- STL – stereolotography

- TAWSS – time-averaged wall shear stress

- UDF – user defined function

- Wo – Womersley number

List of symbols

Latin alphabet

a – average agglomerate size

a_α – left side of eq. 21

agg – agglomerate

agg/s – agglomerate and single red blood cell

$\frac{A_c}{A_0}$ – ratio of crossectional areas in the middle of the constriction and before

b – daughter function

b_α – left side of eq. 22

B^a – birth fuction for agglomeration

B^b – birth fuction for breakage

$B(\vec{x}, t)$ – birth function

C_α – diffusion term in the population balance DQMOM

$\bar{C}_k^{(N)}$ – diffusion term in the DQMOM population balance for a distribution moment of order k

D^a – death fuction for agglomeration

D^b – death fuction for breakage

D_{EFF} – effective diffusion coefficient

d_h – hydraulic diameter

D_M – diffusion coefficient for dense suspension

$D(\vec{x}, t)$ – death fuction

f – frequency

H – hemolysis index

H_L – modified hemolysis index

$\Delta H_b/H_b$ – hemolysis ratio

k – distribution moment order

L – particle size

$M(\phi)$ – relative viscosity

$M_0\ (\phi)$ – relative viscosity for low Pe values

$M_\infty\ (\phi)$ – relative viscosity for high Pe values

m_k – n-th distribution moment

$\widehat{m}_k$ – scaled n-th distribution moment

m_s – 0-th distribution moment for single RBCs

$n(\vec{x}, t)$ – distribution function

s – single red blood cell

$S_L(L)$ – source term in the population balance DQMOM

$\bar{S}_k^{(N)}$ – source term in the population balance DQMOM for a distribution moment of order k

t – time

u – velocity

$u_{pi}(\vec{x}, t)$ – particle velocity

$u_{pj}(\vec{x}, t)$ – internal coordinate change rate

v – substitution symbol in eq. 6

w_α – weight for DQMOM

$\vec{x}$ – vector of external and internal coordinates

x_i –external coordinate

x_j – internal coordinate

Greek alphabet

β – agglomeration kernel

$\dot{\gamma}$ – shear rate

δ – Dirac's delta

Γ – breakage kernel

ϕ – apparent volume fraction

ϕ^* – maximum apparent volume fraction

μ – viscosity

μ_0 – viscosity of reference fluid

ρ – denisty

ς – product of abcissas and weights

τ – shear stress

τ_{max} – maximum shear stress

Introduction

Due to the increasing mortality resulting from complications of circulatory system diseases [1–3], there is a growing need for efficient and modern diagnostics and treatment planning of circulatory system diseases (Fig.1). One of the most common diseases of the circulatory system is atherosclerosis, which is often accompanied by other comorbidities such as hypertension.

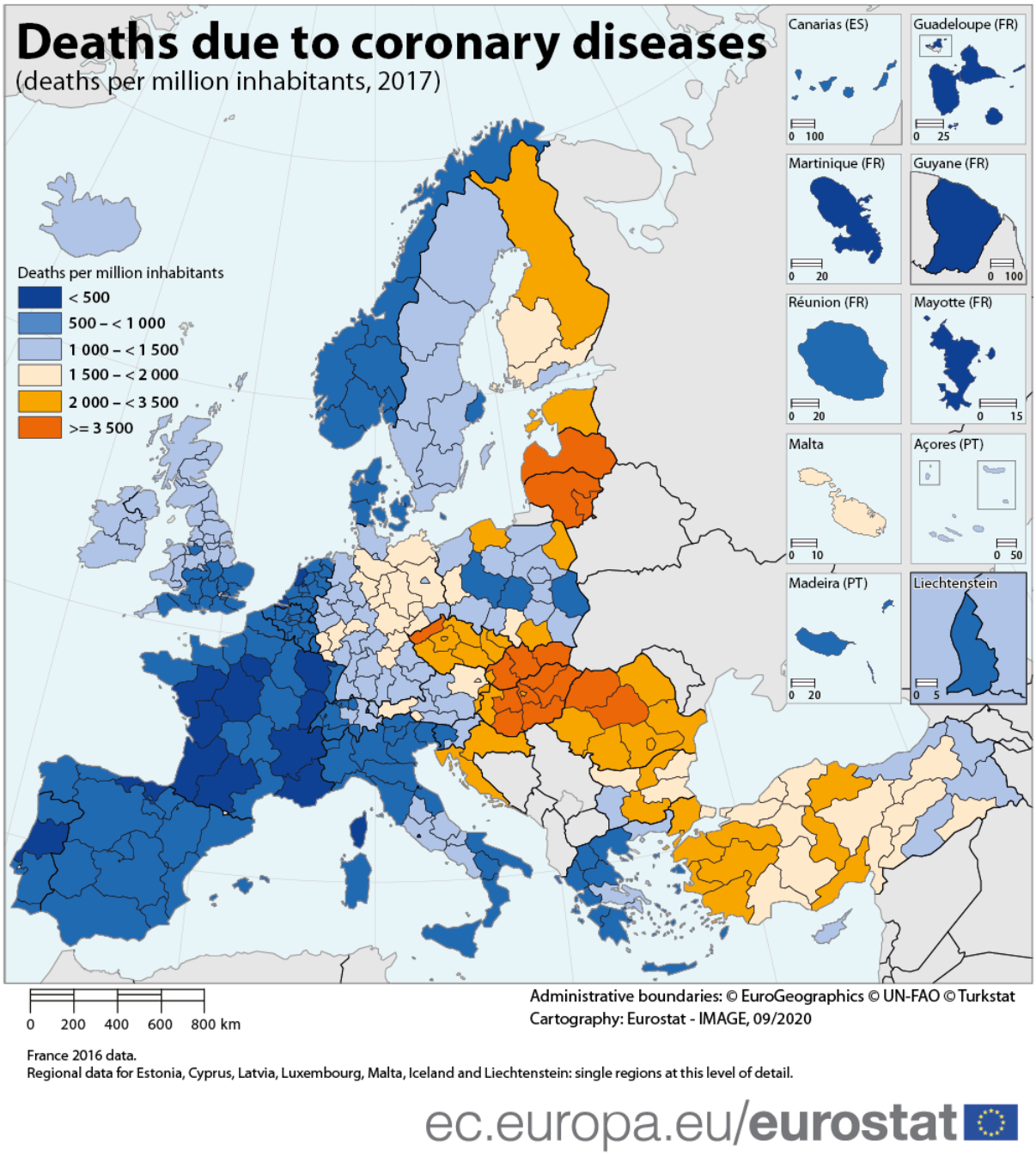

Figure 1. Deaths due to coronary diseases in Europe. [4]

Diseases such as atherosclerosis are often a consequence of an inadequate diet, lack of physical activity, smoking, etc. [5, 6] In patients with atherosclerosis, the accumulated cholesterol causes a reduction in the lumen of the vessels, which causes both an increase in local pressure drops, often reducing blood flow, and consequently leading to hypoxia of organs or muscles, as well as an increase in shear stress in the area of stenosis, which may result in blood hemolysis. Hemolysis caused by high shear stress causes destruction of erythrocytes [7, 8] and, consequently, release of Fe^{2+} ions [9], which may increase the risk of clotting clots, which may block the distal parts of the arteries, creating a risk of hypoxia in further parts of the circulatory system, or may lead to a heart attack or cerebral hypoxia if the flow is blocked at the level of the carotid or cerebral arteries. Currently, the standard in medical practice to assess the risk resulting from the presence of cholesterol constrictions is to measure FFR after prior administration of adenosine [10]. However, this test is an invasive test that requires the insertion of a device into the artery to be examined. Like any invasive test, it involves risks, such as damage to the cholesterol plaque, which, if released, may block further sections of the circulatory system. The current trend in diagnostics is to use non-invasive or least invasive techniques. The development of medical imaging techniques such as computed tomography or magnetic resonance imaging creates hopes for the development of non-invasive medical diagnostics. In parallel with the development of imaging methods, the computing power of computers and their use in medical practice, including in the area of artificial intelligence and CFD simulations, are increasing. Another dynamically developing branch is 3D printing, which is increasingly used in planning the treatment of diseases, especially before major surgical procedures. Printed elements can be used as preview elements for planning the procedure as well as training material to minimize the risk of postoperative complications.

Purpose

The aim of the research conducted as doctoral dissertation was to develop guidelines for physicians to assess the risk of hemolysis in arteries affected by atherosclerosis and to develop a low-cost platform for training complex angioplasty procedures with stent insertion.

Scientific dissertation theses

T1 – Medical imaging such as computed tomography or magnetic resonance imaging allows you to obtain high-quality models of coronary, carotid, and cerebral arteries that can be used in advanced CFD simulations of blood hemolysis in patients with atherosclerosis.

T2 – There is a relationship between the geometric shape of the cholesterol constriction and the maximum shear stress responsible for the risk of mechanical hemolysis that can be determined by CFD calculations and experiments.

T3 – 3D printing allows for high-resolution printing of transparent models of blood vessels to observe the processes inside the phantoms.

T4 – Experimental measurements of blood like flow in printed artery models are possible to verify CFD simulations.

T5 – It is possible to develop a methodology for 3D printing transparent flexible arteries with mechanical properties similar to natural arteries.

Scope

The scope of the research in this work included (I) developing a methodology for processing medical imaging data to create blood vessel models for both CFD simulation and 3D printing; (II) development of preparation of models for 3D printing, 3D printing procedures and 3D printing post-processing; (III) rheological tests and measurements of the refractive index in order to develop blood rheology solutions with a refractive index identical to the refractive index of the 3D print; (IV) development of a new rheological model of blood and hemolysis based on the population balance of red blood cell agglomerates; (V) verification of the correctness of CFD simulations using PIV measurements; (VI) determining the relationship between the shape of the cholesterol constriction geometry and maximum shear stresses; and (VII) development of a system for practicing angioplasty with stent insertion.

In this dissertation, six publications [P1-P6] were summarized and sorted out, presenting the results obtained as a part of doctoral activities. This dissertation has been divided into III parts:

I part – Literature review (chapters 1– 4)

The motivation for undertaking research on this topic is explained in this part of the dissertation. The current state of knowledge related to the diagnosis and treatment planning of atherosclerosis is described. The influence of atherosclerosis on the increased risk of blood hemolysis is presented. The advantages and disadvantages of various medical imaging methods in the context of the diagnosis of cardiovascular diseases are discussed. The current state of technology related to 3D printing in medical applications was shown. Finally, the application of experimental and numerical methods in biomedical applications is presented.

II part – Results and discussion (chapter 5 – 8)

Six publications created during the doctoral activities were summarized and reorganized to form a complete presentation.

III part – Conclusions (chapter 9)

In this part of the dissertation, all research results are summarized and the most important conclusions are drawn. Moreover, this part also contains the answer to the research problems formulated in the research theses.

1. Atherosclerosis

Atherosclerosis is a chronic inflammatory disease of the arteries. It is characterized by the formation of characteristic changes within the vessel walls - atherosclerotic plaques. Atherosclerosis can be both an asymptomatic disease and cause, among other things, coronary pain. Atherosclerosis can develop for many years and is the cause of coexisting cardiovascular diseases, including heart attack. Maintaining an appropriate lifestyle is very important in the prevention of atherosclerosis. An appropriate diet and maintaining an appropriate body weight combined with physical activity significantly reduce the risk of atherosclerosis.

1.1 Lesion classification

Cholesterol deposits within atherosclerotic lesions have a complex structure and partial tissue calcification often occurs. According to the classification of the American Heart Association, there are 6 types of atherosclerotic lesions, as shown in the infographic in Fig. 2.

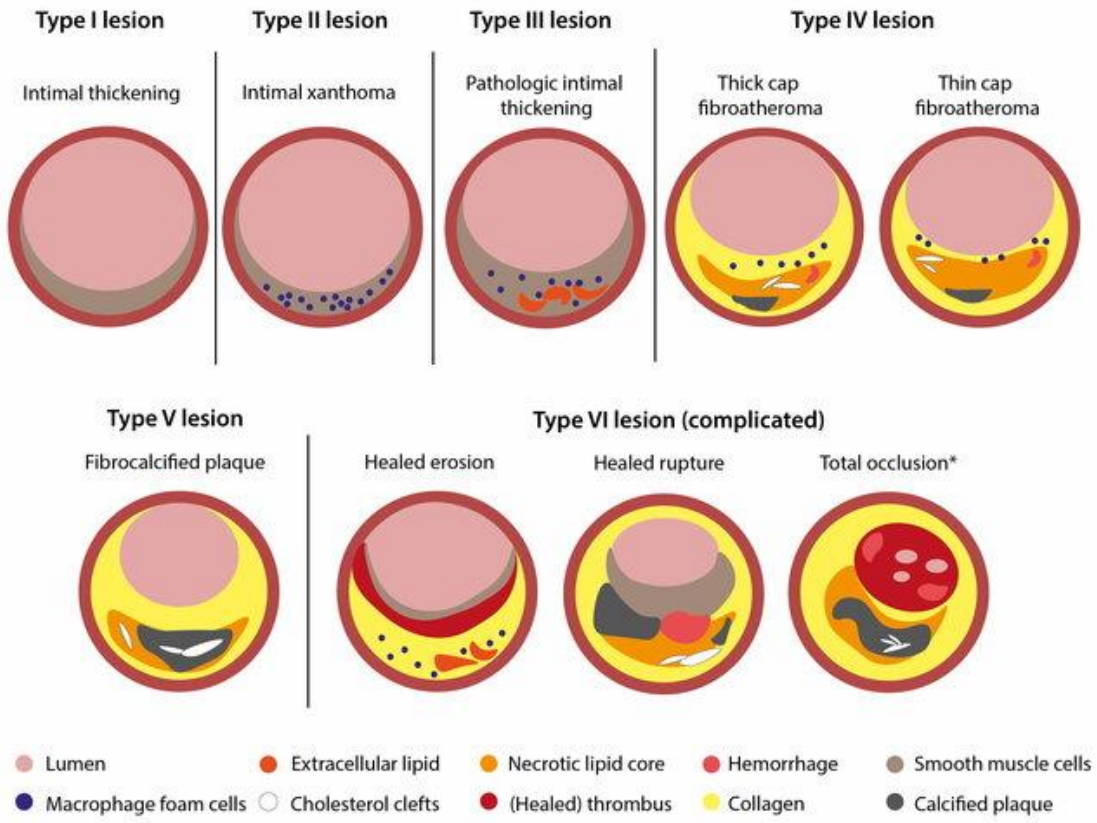

Figure 2. Classification of coronary atherosclerosis. Integrated coronary plaque classification based on the American Heart Association [11] and Virmani schemes [12]. * Total occlusion as resulting from prior thrombi. Figure reproduced from [13] with permission from IMR Press.

In the type I lesion, the intima layer of the artery wall thickens. In the case of type II lesion, intimal xanthoma occurs. In the type III lesion, there is a pathological thickening of the intima layer. In case of type IV lesion thick cap fibroatheroma is visible. Moreover, In case of type V fibrocalcified plaque is formed. The last type VI is complicated lesion. It can be with healed erosion, healed rupture, or even total occlusion.

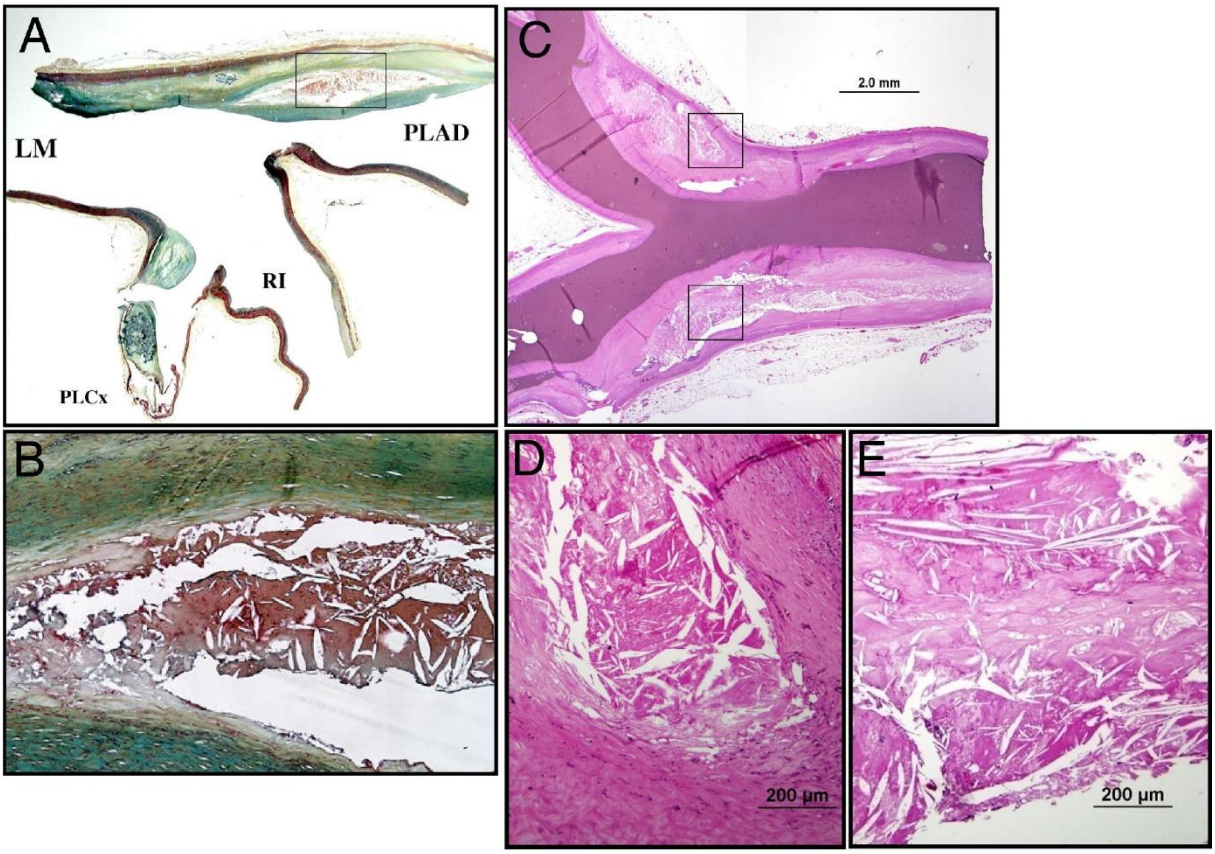

Figure 3. Representative Histologic Images of Coronary Plaque in Bifurcation Lesion (A) Longitudinal section of trifurcation: left main (LM)/proximal left anterior descending coronary artery (PLAD)/ramus intermedicus (RI)/proximal left circumflex (PLCx). (B) Atherosclerotic plaques were observed in the lateral wall, whereas the flow divider regions were spared. (C) Longitudinal section obtained from the region of the LCx/left obtuse marginal bifurcation. Note the severe luminal narrowing proximal and distal to the bifurcation. (D, E) Low-shear regions show atherosclerotic plaque development, including necrotic core formation, whereas flow divider regions (the carina) have minimal intimal thickening. Figure reproduced from [14] with permission from Elsevier.

Figure 3 shows histological images of atherosclerotic tissue, including areas where necrotic core has occurred. Based on the images, it can be seen that the outer vessel wall is preserved, while the inner one is deformed due to the presence of atherosclerotic plaque. This data is

particularly important in the case of FSI simulations or 3D printing realistic models of arteries with atherosclerotic changes, where the increase in the thickness of the vessel wall by the size of the cholesterol lesion must be taken into account.

1.2 Hemolysis

Hemolysis is the process of destroying red blood cells. It can occur naturally according to the erythrocyte life cycle, where they are broken down in the spleen and liver after about 120 days after their formation [15]. However, there is also hemolysis, which is a pathological phenomenon, e.g. as a result of the impact of high shear stresses on the red blood cell membrane, which consequently leads to the rupture of the erythrocyte and the release of its contents. This phenomenon, as its intensity increases, can both lead to anemia and increase the risk of clot formation, which may lead to blockages in blood vessels. The phenomenon of mechanical hemolysis has been analyzed for many years, e.g. in the case of blood pumps, where the rotating elements of the pump can generate high shear stresses. In the case of mechanical hemolysis occurring in the circulatory system, we can mention hemolysis occurring in paravalvular leaks [16–18], which may occur as a pathological phenomenon after heart valve replacement or in the case of serious atherosclerotic stenosis, especially in the case of high physical activity, when the heart pumps blood at a faster rate, generating higher stresses in the stenosis area.

Over the years, many mathematical models have been developed to describe the hemolysis process, such as Power-law equation model [7], Eulerian version of power-law equation model [8, 19], Empirical formulation for blood pumps [20], Lagrangian formulation of the power-law [21], Lagrangian power-law formulation for closed-loop circulations [22], Viscoelastic Lagrangian model [23], Strain-tensor-based Lagrangian models [24–26], Strain-scalar-based Lagrangian model [27], Eulerian strain-tensor-based model [28], Cell-resolved Lagrangian solver [29] and Population balance based rheology (PBBR) model [P1].

1.3 Hypertension

Arterial hypertension is a disease that means long-term high blood pressure above 140/90 mm Hg or more. Classic diagnostics involve several blood pressure measurements performed at intervals of several days or weeks. This disease often coexists with atherosclerosis, causing greater blood flow through the narrowed vessels due to the increased pressure, exposing the body to a greater risk of hemolysis, as high local pressure losses occur in the narrowed areas, which is observed, for example, during Fractional flow reserve (FFR) measurements [10, 30–32].

Risk factors for hypertension include: obesity, high salt intake, aging process, mental stress or low physical activity [33]. Many of the increased risk factors are similar to the risk factors for atherosclerosis. Arterial hypertension is most often treated pharmacologically, and automatic 24-hour blood pressure monitoring, the so-called Holter, is often ordered [34]. Treatment of hypertension is often necessary until the end of life in order to reduce the risk of further complications such as heart attack, heart failure, stroke or vascular or kidney damage. In addition to pharmacological treatment, it is important to change the lifestyle, increase physical activity, change the diet to e.g. the Mediterranean diet, limit or give up alcohol consumption and reduce salt consumption.

2. Medical imaging

The beginnings of medical imaging are basically associated with two events: the discovery of X-ray radiation in 1895 by the German scientist Wilheml Röntgen and the first X-ray image of the entire human body taken in 1934 by Arthur Fuchs from the American company Kodak. The next imaging method that was developed was ultrasound examination (USG) in 1945. This was followed by the development of computed tomography in 1968 [35], and a nine years later in 1977 magnetic resonance imaging.

Currently, many medical imaging techniques are used, in the case of the circulatory system, it is worth mentioning such techniques as optical coherence tomography [36–40], near-infrared spectroscopy [41], ultrasound imaging [42–45], computed tomography [46–52], and magnetic resonance imaging [52–58].

2.1 Computed tomography (CT)

Computed tomography is a non-invasive procedure that involves a series of X-rays in a camera that takes pictures as it rotates around the patient's axis, resulting in a series of pictures. These tests should be used in moderation due to the patient's exposure to ionizing radiation, which in large doses increases the risk of cancer. These tests are characterized by high resolution and are widely used in diagnostics. Contrast is often administered to increase image contrast, because without it the difference in density between the blood and the vessel walls is sometimes insufficient.

A related imaging technique is microCT, which is used on smaller samples, including those taken from humans or animals, often post-mortem. The microCT examination allows for much higher resolutions than classic CT at the expense of a smaller sample and greater exposure to

radiation. An even more advanced technique is nanoCT, where submicron resolutions can be obtained, but at the expense of an even smaller scan volume of the sample.

2.2 Magnetic resonance imaging (MRI)

Magnetic resonance imaging uses a magnetic field to produce images as the camera rotates, similar to a CT scan. MRI imaging is better at imaging soft tissue compared to CT. This test does not involve the risk of exposure to ionizing radiation, so it is safer. However, due to the presence of a strong electromagnetic field, patients with implanted metal prostheses or electronic devices cannot use this test. The classic MRI machine is a horizontal machine in which the patient enters the machine in a lying position. There are also vertical cameras that allow measurements in the NMR spectroscope mode. These devices are used for microimaging due to the greater spatial resolution but limited sample volume.

A new emerging MRI technology is 4D flow MRI [57–63], which allows for the analysis of blood flow to determine the distribution of blood flow in the heart cells or arteries. This technology is extremely promising when planning procedures related to the treatment of cardiac morphology pathologies in young children, where, for example, a double-ventricular heart reconstruction procedure or the Fontan procedure [64] is necessary.

3. Population balance

Population balance is a convenient method to describe a set (population) of elements with high variability of parameters, such as drops in a gas or bubbles in a liquid. Objects are characterized by external parameters such as location or internal parameters - characteristic size, specific surface area or volume. Describing each individual would be difficult and numerically expensive. In such cases, a population balance that statistically captures all individuals by approximating their set through a finite representation of their statistical distribution is helpful. The population balance can be written in general form according to equation (1).

$$\frac{\partial n(\vec{x},t)}{\partial t}+\sum_{i}\frac{\partial u_{pi}(\vec{x},t)n(\vec{x},t)}{\partial x_i}+\sum_{j}\frac{\partial u_{pj}(\vec{x},t)n(\vec{x},t)}{\partial x_j}=B(\vec{x},t)-D(\vec{x},t) \tag{1}$$

3.1 Agglomeration

Agglomeration is a mechanism in which particles combine to form larger structures - agregates, which can also create even larger branched structures - agglomerates. This causes a significant increase in the effective apparent volume fraction of particles, which translates into

a change in rheological parameters. According to the literature, agglomerations of particles with mass m and μ can be described according to equations (2-3):

$$B^a = \frac{1}{2}\int_0^m \beta(m-\mu,\mu)n(m-\mu)n(\mu)d\mu \tag{2}$$

$$D^a = n(m)\int_0^\infty \beta(m,\mu)n(\mu)d\mu \tag{3}$$

where $n(m)$ is particle density function and $\beta(m,\mu)$ is agglomeration kernel.

Assuming that the particle mass m is proportional to the characteristic size L and λ in the 3rd power, the equations (2-3) can be rewritten to equations (4-5):

$$B^a(L,\vec{x},t) = \frac{L^2}{2}\int_0^L \frac{\beta(L^3-\lambda^3,\lambda)}{(L^3-\lambda^3)^{2/3}} n\left[(L^3-\lambda^3)^{1/3},t\right]n(\lambda,t)d\lambda \tag{4}$$

$$D^a(L,\vec{x},t) = n(L,t)\int_0^\infty \beta(L,\lambda)n(\lambda,t)d\lambda \tag{5}$$

By introducing the auxiliary variable v^3 according to equation (6)

$$v^3 = L^3 - \lambda^3 \tag{6}$$

and substituting into equations (4) and (5), we can obtain the birth and death functions in distribution moment equation:

$$\overline{B_k^a(L,\vec{x},t)} = \frac{1}{2}\int_0^\infty n(\lambda,t)\int_0^\infty \beta(v,\lambda)n(u,t)(v^3+\lambda^3)^{k/3}dvd\lambda \tag{7}$$

$$\overline{D_k^a(L,\vec{x},t)} = \int_0^\infty L^k\, n(L,t)\int_0^\infty \beta(L,\lambda)n(\lambda,t)d\lambda\, dL \tag{8}$$

3.2 Deagglomeration

Breakage is a mechanism in which agglomerates divide into smaller fragments under the influence of shear stress. This causes a decrease in the effective apparent volume fraction of particles, which translates into a change in rheological parameters. According to the literature, the decay of particles with mass m and μ can be described according to equations (9) and (10):

$$B^b = \int_L^\infty \Gamma(\mu)b(m/\mu)n(\mu,t)d\mu \tag{9}$$

$$D^b = \Gamma(m)n(m,t) \tag{10}$$

where Γ is breakage kernel and $b(m/\mu)$ is daughter distribution function.

By transforming equations (9) and (10) from the dependence on their masses to the dependence on the characteristic sizes L and λ, one can obtain equations for birth and death functions in distribution moment equation:

$$\overline{B_k^b(\vec{x},t)} = \int_0^\infty L^k \int_0^\infty \Gamma(\lambda) b(L/\lambda) n(\lambda,t) d\lambda dL \tag{11}$$

$$\overline{D_k^b(\vec{x},t)} = \int_0^\infty L^k \Gamma(L) n(\lambda,t) dL \tag{12}$$

3.3 QMOM

The Quadrature Method of Moments (QMOM) uses an approximation of the continuous distribution of population parameters by a discrete distribution in the form of Dirac deltas as in equation (13). Set

$$n(L) \cong \sum_{\alpha=1}^{N} w_\alpha \delta(L - L_\alpha) \tag{13}$$

The population distribution moment of order k can be defined according to equation (14)

$$m_k = \int_0^\infty n(L) L^k dL \tag{14}$$

Using the approximation from equation (13), equation (14) for a population moment of order k can be written as equation (15).

$$m_k = \sum_\alpha w_\alpha L_\alpha^k \tag{15}$$

The QMOM can be easily implemented in CFD codes using user defined functions (UDF) [65] and scalar balances, available, for example, in ANSYS Fluent software. Unfortunately, spatial discretization for orders above the first one is problematic because moment corruption may occur. There are various techniques that can partially circumvent this problem, but they are more complicated to implement and may not fully guarantee the stability of the calculations.

3.4 DQMOM

Another method developed by Marchisio and Fox [66] is the Direct Quadrature Methods of Moments (DQMOM). This method, instead of balancing moments, balances weights w_α and the product of weights w_i and abscissas L_α. Equation (1) can be written in the equivalent form according to equation (16):

$$\frac{\partial n(L)}{\partial t} + \frac{\partial}{\partial x_i}\left(\bar{u_\iota} n(L)\right) - \frac{\partial}{\partial x_i}\left(D_{EFF}\frac{\partial n(L)}{\partial x_i}\right) = S_L(L) \tag{16}$$

Substituting the moment definition according to equation (15) into $n(L)$ from equation (16) allows us to obtain equation (17) for the balance of population moments.

$$\frac{\partial \sum_\alpha w_\alpha L_\alpha^k}{\partial t} + \frac{\partial}{\partial x_i}\left(\bar{u_\iota}\sum_\alpha w_\alpha L_\alpha^k\right) - \frac{\partial}{\partial x_i}\left(D_{EFF}\frac{\partial \sum_\alpha w_\alpha L_\alpha^k}{\partial x_i}\right) = S_L(L) \tag{17}$$

By transforming equation (17) and using the definition of the derivative of the Dirac delta function and (13), equation (18) can be obtain

$$\begin{aligned}\sum_\alpha \delta(L-L_\alpha)\left[\frac{\partial w_\alpha}{\partial t} + \frac{\partial}{\partial x_i}(\bar{u}_i w_\alpha) - \frac{\partial D_{EFF}}{\partial x_i}\frac{\partial w_\alpha}{\partial x_i} - D_{EFF}\frac{\partial^2 w_\alpha}{\partial x_i^2}\right] \\ -\sum_\alpha \delta'(L-L_\alpha)\left[w_\alpha\frac{\partial L_\alpha}{\partial t} + w_\alpha\frac{\partial}{\partial x_i}(\bar{u}_i L_\alpha) - w_\alpha\frac{\partial L_\alpha}{\partial x_i}\frac{\partial D_{EFF}}{\partial x_i}\right. \\ \left. - D_{EFF}\frac{\partial w_\alpha}{\partial x_i}\frac{\partial L_\alpha}{\partial x_i} - D_{EFF}\frac{\partial^2 L_\alpha}{\partial x_i^2} - D_{EFF}\frac{\partial w_\alpha}{\partial x_i}\frac{\partial L_\alpha}{\partial x_i}\right] \\ -\sum_\alpha \delta''(L-L_\alpha)\left[D_{EFF} w_\alpha\frac{\partial L_\alpha}{\partial x_i}\frac{\partial L_\alpha}{\partial x_i}\right] = S_L(L)\end{aligned} \tag{18}$$

By introducing an auxiliary variable ς_α in equation (19):

$$\varsigma_\alpha = w_\alpha L_\alpha \tag{19}$$

equation (20) can be get

$$\begin{aligned}\sum_\alpha \delta(L-L_\alpha)\left[\frac{\partial w_\alpha}{\partial t} + \frac{\partial}{\partial x_i}(\bar{u}_i w_\alpha) - \frac{\partial}{\partial x_i}\left(D_{EFF}\frac{\partial w_\alpha}{\partial x_i}\right)\right] \\ -\sum_\alpha \delta'(L-L_\alpha)\left\{\frac{\partial \varsigma_\alpha}{\partial t} + \frac{\partial}{\partial x_i}(\bar{u}_i \varsigma_\alpha) - \frac{\partial}{\partial x_i}\left(D_{EFF}\frac{\partial \varsigma_\alpha}{\partial x_i}\right)\right. \\ \left. - L_\alpha\left[\frac{\partial w_\alpha}{\partial t} + \frac{\partial}{\partial x_i}(\bar{u}_i w_\alpha) - \frac{\partial}{\partial x_i}\left(D_{EFF}\frac{\partial w_\alpha}{\partial x_i}\right)\right]\right\} \\ -\sum_\alpha \delta''(L-L_\alpha)\left[D_{EFF} w_\alpha\frac{\partial L_\alpha}{\partial x_i}\frac{\partial L_\alpha}{\partial x_i}\right] = S_L(L)\end{aligned} \tag{20}$$

Lets introduce auxiliary variables a_α and b_α in equations (21) and (22)

$$\frac{\partial w_\alpha}{\partial t} + \frac{\partial}{\partial x_i}(\bar{u}_i w_\alpha) - \frac{\partial}{\partial x_i}\left(D_{EFF}\frac{\partial w_\alpha}{\partial x_i}\right) = a_\alpha \tag{21}$$

$$\frac{\partial \varsigma_\alpha}{\partial t} + \frac{\partial}{\partial x_i}(\bar{u}_i \varsigma_\alpha) - \frac{\partial}{\partial x_i}\left(D_{EFF} \frac{\partial \varsigma_\alpha}{\partial x_i}\right) = b_\alpha \tag{22}$$

and also auxiliary variables C_α in equation (23)

$$C_\alpha = D_{EFF} w_\alpha \frac{\partial L_\alpha}{\partial x_i} \frac{\partial L_\alpha}{\partial x_i} \tag{23}$$

then equation (20) can be rewritten into equation (24)

$$\sum_\alpha [\delta(L - L_\alpha) - \delta'(L - L_\alpha)] a_\alpha - \sum_\alpha \delta'(L - L_\alpha) b_\alpha = \sum_\alpha \delta''(L - L_\alpha) C_\alpha + S_L(L) \tag{24}$$

Using equations (25-27),

$$\int_{-\infty}^{\infty} L^k \, \delta(L - L_\alpha) dL = L_\alpha^k \tag{25}$$

$$\int_{-\infty}^{\infty} L^k \, \delta'(L - L_\alpha) dL = -k L_\alpha^{k-1} \tag{26}$$

$$\int_{-\infty}^{\infty} L^k \, \delta''(L - L_\alpha) dL = k(k-1) L_\alpha^{k-2} \tag{27}$$

equation (24) can be written in a new form, equation (28)

$$(1 - k) \sum_\alpha L_\alpha^k a_\alpha + k \sum_\alpha L_\alpha^{k-1} b_\alpha = \bar{S}_k^{(N)} + \bar{C}_k^{(N)} \tag{28}$$

where

$$\bar{S}_k^{(N)} = \int_0^{\infty} L^k S_L(L) dL \tag{29}$$

and

$$\bar{C}_k^{(N)} = k(k-1) \sum_\alpha L^{k-2} C_\alpha \tag{30}$$

4. Fluid mechanics in cardiovascular medicine

Fluid mechanics is a branch of continuous media mechanics dealing with the analysis of the movement of fluids, i.e. liquids and gases. Mathematical tools provided by fluid mechanics allow for the mathematical description of the movement of fluids both in pipelines used in

industry and the description of flow in, for example, oceanography, weather forecasting or medicine. Fluid mechanics can be divided into two branches, experimental fluid mechanics based on experiments and computational fluid mechanics, where the analysis is performed in silico.

4.1 Application of CFD simulations in cardiovascular medicine

Computational fluid dynamics (CFD), together with the development of computer computing power and the increase in the resolution of medical imaging techniques, is becoming an increasingly used tool in analyzing the functioning of the circulatory system. In CFD, it is crucial to have accurate boundary conditions for the simulation in order to perform the numerical analysis correctly. In this case, information about pressure or flow with the highest possible time resolution is useful. In the case of flow, information from Doppler Ultrasound measurements or information from 4D flow MRI is useful [59]. The information obtained from experimental measurements should then be implemented either by directly implementing a flow or pressure profile or by using 0-dimensional models reflecting the work of the circulatory system system [67] or, for example, the Windkessel model [68] often used as a boundary condition for the arterial system.

Currently, CFD is used, among others, in modeling blood flow in the heart chambers, aorta, coronary, carotid, cerebral and other arteries, in the analysis of procedures such as ECMO [69], in the design of new blood pumps, the impact of stents [70] in the human body on the flow in arteries, and many others.

4.2 Application of experimental fluid mechanics in cardiovascular medicine

Experimental fluid mechanics in cardiovascular medicine is used to study the functioning of the circulatory system or to verify numerical simulations. A useful measurement technique for analyzing flow in phantoms of circulatory system elements is particle image velocimetry (PIV). In the literature can be found many applications of various variants of PIV measurements, such as 2D PIV [71, 72], Stereoscopic (2D3C) PIV [73], Tomographic PIV (3D3CPIV) [74], Echo PIV (EPIV) [75, 76], Smartphone-based PIV [77] or X-ray PIV [78]. The mentioned techniques often require the development of appropriate phantom models of the circulatory system components; 3D printing technique is often used in this case [79]. In the preparation of phantoms of circulatory system elements, 3D printing methods such as Material Jetting (PolyJet) [80], stereolithography (SLA) [72, 81], Fused Deposition Modeling (FDM) [81], Powder Bed Fusion (PBF) [82] or Binder Jetting [83, 84] are useful. 3D printing

techniques may allow for direct printing of a model or printing of a mold that can be filled with e.g. silicone or epoxy resin to ensure an appropriate level of transparency.

5. Population balance based rheology

The population balance rheology model is based on the assumption that the main blood component suspended in the plasma are erythrocytes, which can agglomerate depending on local shear stresses. The model assumes that the dominant mechanism of agglomerate breakage is erosion. In addition to accounting for agglomeration and deagglomeration of red blood cells, the model takes into account hemolysis of fully deagglomerated red blood cells if shear stresses exceed 150 Pa [P1]. The model was developed based on previous rheological models of silica suspensions based on population balance [85–87], taking into account differences in the specificity of blood rheology and the behavior of red blood cells. The developed model allows for the mapping of the effect of blood shear thinning and its thixotropic effects related to the finite rate of agglomeration and deagglomeration of red blood cells.

5.1 Derivation of the population balance model

The general form of the population balance according to QMOM containing all birth and death functions for the deagglomeration and agglomeration processes in all possible combinations in the case of the balance of red blood cell agglomerates can be written according to equation (31).

$$\begin{aligned}&\frac{\partial m_k}{\partial t}+\frac{\partial}{\partial x_i}(\overline{u_i}m_k)-\frac{\partial}{\partial x_i}\left(D_{EFF}\frac{\partial m_k}{\partial x_i}\right)\\&=\frac{1}{2}\sum_i w_i\sum_j w_j\left(L_i^3+L_j^3\right)^{k/3}\beta_{ij}-\sum_i L_i^k w_i\sum_j \beta_{ij}w_j\\&+\sum_i \Gamma_i b_i^{(k)}-\sum_i \mathrm{L_i^k}\Gamma_i w_i+m_s\sum_i (L_i^3+L_0^3)^{k/3}\beta_{si}w_i\\&-m_s\sum_i L_i^k w_i\beta_{si}+(L_0^3+L_0^3)^{k/3}m_s^2\beta_{ss}\end{aligned} \tag{31}$$

and equation (32) [P1]

$$\frac{\partial m_s}{\partial t}+\frac{\partial}{\partial x_i}(\overline{u_i}m_s)-\frac{\partial}{\partial x_i}\left(D_{EFF}\frac{\partial m_s}{\partial x_i}\right)=\sum_i \Gamma_i w_i-m_s\sum_i w_i\beta_{si}-2m_s^2\beta_{ss} \tag{32}$$

In order to improve the stability of calculations, it is worth considering the normalization of moments to improve the stability of calculations in accordance with equation (33)

$$\zeta_i = \frac{L_i}{L_0} \tag{33}$$

then the population balance moment can be written as in equation (34)

$$m_k = \sum_i w_i (\zeta_i L_0)^k = {L_0}^k \sum_i w_i {\zeta_i}^k = L_0^k \widehat{m}_k \tag{34}$$

which finally gives the formula for the normalized moment of population balance according to equation (35)

$$\widehat{m}_k = L_0^{-k} m_k \tag{35}$$

Using the normalization procedure and transformations from the QMOM to DQMOM equations as presented earlier, it is possible to obtain the equations presented in [P1].

5.2 Viscosity model

The viscosity model is based on the fact that with the process of agglomeration and deagglomeration of red blood cells, the apparent volume fraction of RBCs ϕ changes. This is due to the change in shape and complexity of the agglomerates, which are larger and more complex in low shear rate regions. The model was first presented in [P1] for a hematocrit of 45%, and in [P2] a modification generalizing the model to the full range of physiological hematocrits was presented:

$$\mu = M(\phi)\mu_0 \tag{36}$$

where $\mu_0 = 6.99 \cdot 10^{-4}$ Pa s is the viscosity obtained by fitting viscosity experimental data [P1].

$M(\phi)$, the relative blood viscosity, is defined as follows [P1]

$$M(\phi) = \frac{M_0(\phi) + Pe M_\infty(\phi)}{1 + Pe} \tag{37}$$

and the Peclet number, Pe, is defined as follows [P1].

$$Pe = \frac{\dot{\gamma} a^2}{D_M(\phi)} \tag{38}$$

$M_\infty(\phi)$, the relative blood viscosity for high shear rates, is determined using (39) [P1].

$$M_\infty(\phi) = (1-\phi)^{-5/2} - C\left\{\ln\left[1 - \left(\frac{\phi}{\phi^*}\right)^{1/3}\right] + \sum_{j=1}^{6} \frac{1}{j}\left(\frac{\phi}{\phi^*}\right)^{j/3}\right\} \tag{39}$$

$M_0(\phi)$, the relative blood viscosity for low shear rates, is determined using (40): [P1].

$$M_0(\phi) = (1-\phi)^{-5/2} + 1.3\left[\left(1-\frac{\phi}{\phi^*}\right)^{-2} - \sum_{j=0}^{2}(1+j)\left(\frac{\phi}{\phi^*}\right)^{j}\right] \tag{40}$$

where $\dot{\gamma}$ is the shear rate, a is the characteristic particle size for the entire population and is equal to the volume-weighted mean particle size, ϕ is the effective apparent volume fraction of RBCs, $D_M(\varphi)$ is the effective diffusion coefficient [88] for molecular diffusion, C ≅ 2 and is equation constant, and ϕ^* is the maximum apparent volume fraction equal to 0.695 [85, 87, 88].

The PBBR model predicts the viscosity increase well at low shear rates, as shown in [P1] by comparing it with other models such as Carreau [89], Carreau Yasuda [90], Power-law [91] or Cross [92], as well as experimental data [93–95]. Publication [P1] also shows the thixotropic effects of blood that the PBBR model can predict and comments on it in relation to thixotropic blood models [96–101] known in the literature. Publication [P1] also presents a comparison of the results for the flow through a model arterial narrowing for the PBBR model and the Careau Yasuda model. Moreover, in [P2] the application of the model is discussed in more detail for, among others, lower hematocrits, where the influence of other blood components is more important.

5.3 Hemolysis model

The model of mechanical hemolysis of red blood cells is based on the assumption that only single red blood cells can hemolyze. However, hemolysis of single blood cells can be described by a power law relationship similar to the one proposed by Giersiepen et al. [7]:

$$H = 3.62 \cdot 10^{-7}\tau^{2.416}t^{0.785} \tag{41}$$

where H is the hemolysis index, τ is the shear stress, and t is time.

Unfortunately, Giersiepen's formula cannot be implemented in CFD code in its classical form due to its non-linear term; however, this can be bypassed [8] and rewritten as:

$$H_L = A\tau^{\theta}t, \tag{42}$$

with

$$H_L = H^{\frac{1}{\beta}}, A = (3.62 \cdot 10^{-7})^{\frac{1}{\beta}} \tag{43}$$

$$\theta = \frac{\alpha}{\beta}, \alpha = 2.416, \beta = 0.785$$

where H_L is the modified hemolysis index and α, β, θ, A are the model constants.

The PBBR model considers the convection and diffusion of hemolyzed cells [P1]. Further, an additional term $(1 - H_L)$ was added to take into account only nonhemolyzed cells [19].

$$\frac{\partial H_L}{\partial t} + \frac{\partial}{\partial x_i}(\bar{u}_i H_L) - \frac{\partial}{\partial x_i}\left(D_{EFF}\frac{\partial H_L}{\partial x_i}\right) = \delta A \tau^{\theta}(1 - H_L) \tag{44}$$

where D_{EFF} is the effective diffusion coefficient for molecular and turbulent and

$$\delta = \begin{cases} 0, if\ \tau < \tau_s \\ 1, if\ \tau \geq \tau_s \end{cases} \tag{45}$$

The value of shear threshold τ_s was set to 150 Pa in accordance with recommendations from the literature [102–105].

Additionally, $\Delta H_b/H_b$ was defined as the ratio of hemolyzed single RBCs to total RBCs, including single RBCs and agglomerates, as presented in Eq. (46).

$$\Delta H_b/H_b = \frac{H \cdot m_s L_0^3}{m_s L_0^3 + \sum_{\alpha=1}^{3} w_\alpha L_\alpha^3} \tag{46}$$

where m_s is the number concentration of single red blood cells in Direct Quadrature Method of Moments (DQMOM), L_α are the sizes of agglomerates used in DQMOM, and w_α are the weights used in DQMOM.

5.4 Model programming

The PBBR model was implemented into the ANSYS Fluent computing package using user-defined functions (UDF) written using C++ language. Macros such as define_adjust, define_source, define_property and define_diffusivity were used, among others, in accordance with the guidelines from ANSYS UDF Manual [65]. Details can be found in [P1].

6. Numerical analysis of blood flow

Numerical analysis of blood flow using computational packages in the ANSYS Fluent environment requires the preparation of computational meshes with appropriate parameters of skewness, orthogonal quality and aspect ratio to ensure the correctness of the calculations. In addition, it is very important to determine the flow regime, which is determined by the Reynolds number Re, according to equation (47)

$$\mathrm{Re} = \frac{u d_h \rho}{\mu} \tag{47}$$

where u is the mean velocity of the fluid, d_h is the hydraulic diameter of the vessel, ρ is the density of the blood and μ is the dynamic viscosity of the blood.

Blood flow is a pulsatile flow due to the work of the heart, which consists in rhythmic contraction and relaxation of the heart, and the significance of pulsations can be determined based on the Womersley number, Wo according to equation (48)

$$\mathrm{Wo} = d_h \sqrt{\frac{\pi f \rho}{2\mu}} \tag{48}$$

where f is the frequency of the blood flow pulsation.

The article [P2] examined the importance of taking into account pulsations in modeling the flow through arteries with atherosclerotic narrowings and compared the results of the Time-Averaged Wall Shear Stress (TAWSS) defined in accordance with equation (49) and the shear stress for the average flow over time for steady conditions.

$$\mathrm{TAWSS} = \frac{\int_0^T |\vec{\tau}| dt}{\int_0^T dt} \tag{49}$$

Additionally, the values of parameter such as Oscillatory Shear Index (OSI) defined in accordance with equation (50) was analyzed

$$\mathrm{OSI} = 0.5 \left(1 - \frac{\left| \int_0^T \vec{\tau} dt \right|}{\int_0^T |\vec{\tau}| dt} \right) \tag{50}$$

and Relative Residence Time (RRT) defined in accordance with equation (51) was also analyzed

$$\mathrm{RRT} = \frac{1}{(1 - 2 \cdot OSI) \cdot TAWSS} \tag{51}$$

Figures 4 and 5 show the comparison of TAWSS and shear stress for mean blood flow [P2]. The article [P2] was created in cooperation with the Medical University of Silesia in Katowice, which provided support from a medical perspective.

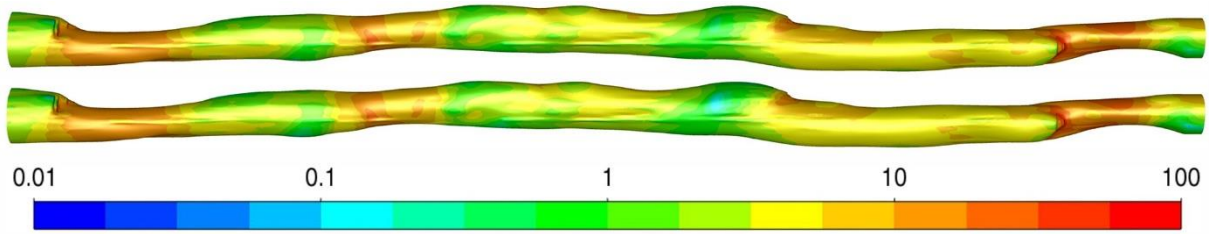

Figure 4. Comparison of the shear stresses (Pa) on the wall for the transient simulation (top) with the case for the mean velocity (bottom)—CT-1 (blood flows from left to right). [P2]

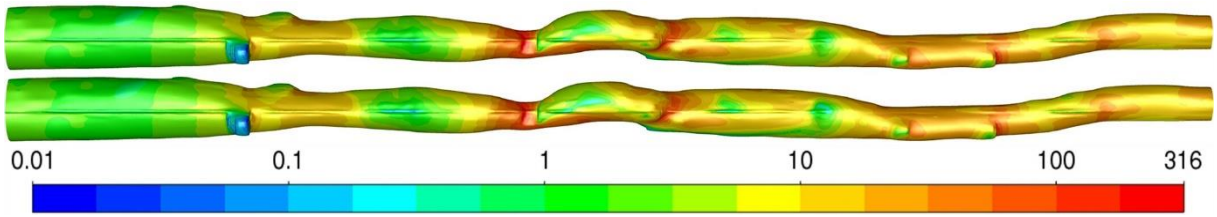

Figure 5. Comparison of the shear stresses (Pa) on the wall for the transient simulation (top) with the case for the mean velocity (bottom)—CT-2 (blood flows from left to right). [P2]

Comparing the results for both geometries in Figures 4 and 5, almost identical results can be seen, although the upper figure from both pairs shows average values for the entire pulsation cycle, and the lower figure corresponds to the flow determined in time for the averaged blood flow. The obtained convergence of results proves that in order to quickly analyze the shear stresses acting on the vessel wall, which are associated with the risk of mechanical hemolysis, it is possible to limit the analysis of the flow steady in time to the average value of blood flow, which significantly reduces the simulation time, allowing for a quick analysis of the patient's condition.

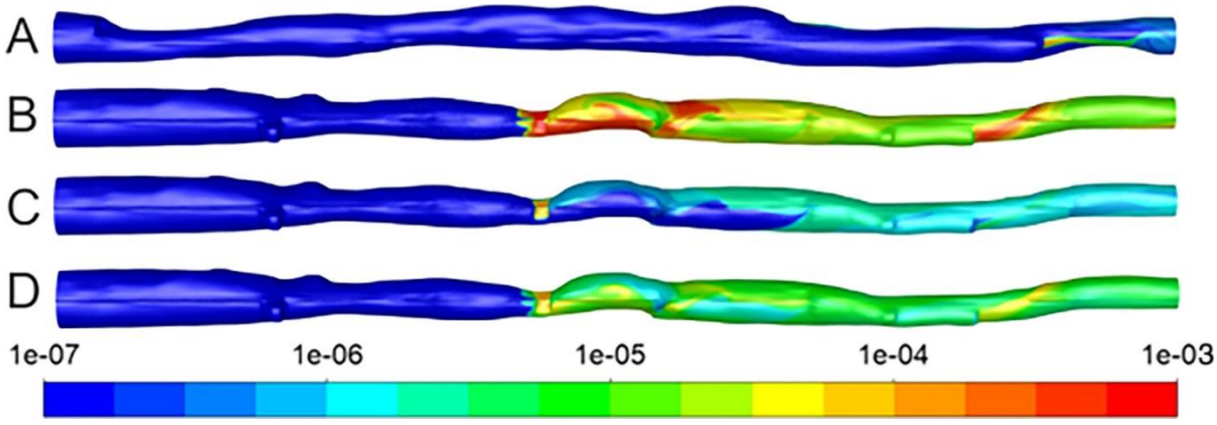

Figure 6. Comparison of the hemolysis ΔHb/Hb (fraction of hemolyzed blood cells). (A) First artery—systolic inlet velocity. (B) Second artery—systolic inlet velocity. (C) Second artery—

mean inlet velocity. (D) Second artery—time-averaged ΔHb/Hb for systole and diastole phase (blood flows from left to right). [P2]

Figure 6 shows a comparison of hemolysis values for steady-state and unsteady-state flows. It can be seen that an increase in flow speed significantly increases the risk of hemolysis because the maximum shear stresses and the area in which they are above 150 Pa increase. It is worth noting that while there is no significant difference between TAWSS and stresses for averaged steady-state flow, in the case of hemolysis itself, it can be seen that in the case of pulsatile flow the risk of hemolysis is greater than in the case of time-averaged flow for average blood flow. This is related to the non-linear relationship between the risk of hemolysis and shear stress and the fact that there is a shear stress threshold that must be exceeded for hemolysis of red blood cells to occur.

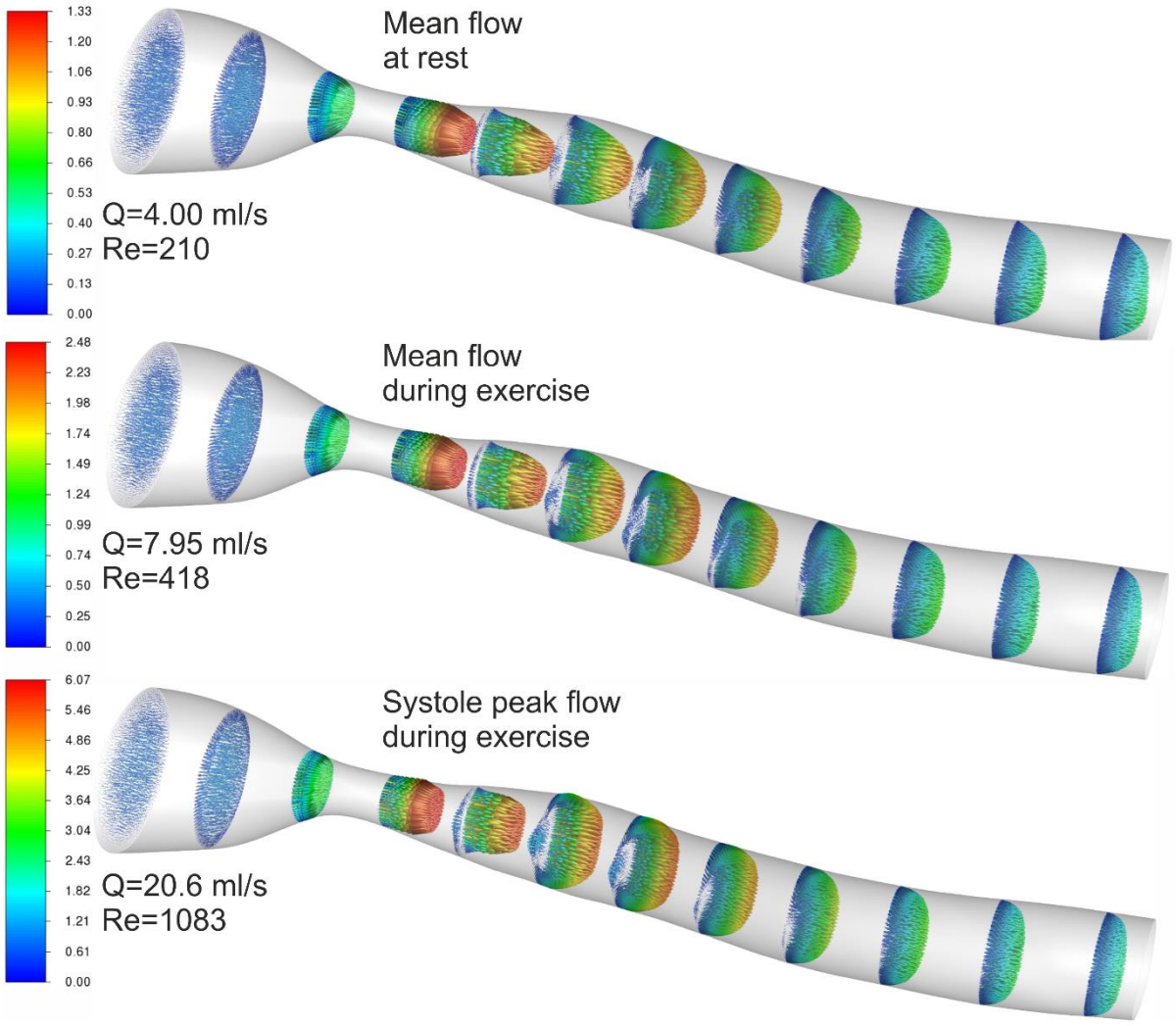

Figure 7. 3D velocity magnitude [m/s] profile results for rest and exercise [P4].

Paper [P4] was created in cooperation with the Military Institute of Medicine—National Research Institute in Warsaw and the Medical University of Silesia in Katowice who were responsible for the medical part of the article. Figure 7 shows the influence of changes in blood flow values on the change in the nature of the flow towards turbulent/transient flow. As the flow increases, the velocity profile in the carotid artery narrowing flattens and the recirculation zone in the space behind the narrowing increases. The increase in shear stress in the cholesterol constriction area combined with the enlargement of the recirculation zone behind the constriction correlates with an increase in the risk of clot formation, which can block blood vessels in the distal part of the circulatory system.

6.1 Preparations of 3D models from medical imaging data

3D artery models used in CFD analysis most often come from data obtained from computed tomography or magnetic resonance imaging. Raw data is most often saved to the DICOM format, commonly used by doctors and specialists in related fields. There are many programs that are used to analyze DICOM files, there are both paid programs such as Materialise Mimics, RadiAnt and open source programs such as InVesalius or 3D Slicer. In order to perform CFD simulation, three-dimensional models of arteries should be created based on medical imaging and exported in e.g. STL format to CAD software. The 3D model must then be carefully inspected to remove any errors, often in the form of needle-like structures or holes resulting from either insufficient resolution or 3D reconstruction errors. At the stage of cleaning the geometry from surface errors, programs such as MeshMixer or ANSYS SpaceClaim are useful. After appropriate preparation of the 3D model, you can focus on isolating interesting parts of the circulatory system in order to create clearly defined inlet and outlet surfaces, where appropriate boundary conditions will be set.

6.2 Hemolysis risk map based on CFD simulations

The article [P3] was prepared in cooperation with the Medical University of Silesia in Katowice, who advised on medical matters. As part of a series of articles, especially articles [P3] and [P4], a hemolysis risk map was developed allowing for the estimation of the risk of hemolysis. The article [P3] focused on the impact of the degree of cholesterol constriction on the risk of hemolysis and examined whether the eccentricity of the constriction also has a significant impact. Moreover, in the article [P4] the analysis was extended to include various narrowing proportions in order to generalize the relationship and it was compared with the simulation results for the patient's carotid artery. The visible results indicate that below 70%

vessel occlusion [106] there is no significant increase in the risk of hemolysis, which is in line with the recommendations of the American Heart Association not to perform angioplasty for arteries with smaller narrowings due to the increasing risk of restenosis [107] with each subsequent stent. However, when occlusion increases to 85%, from that moment on, a rapid increase in shear stress and the risk of hemolysis and other complications is observed.

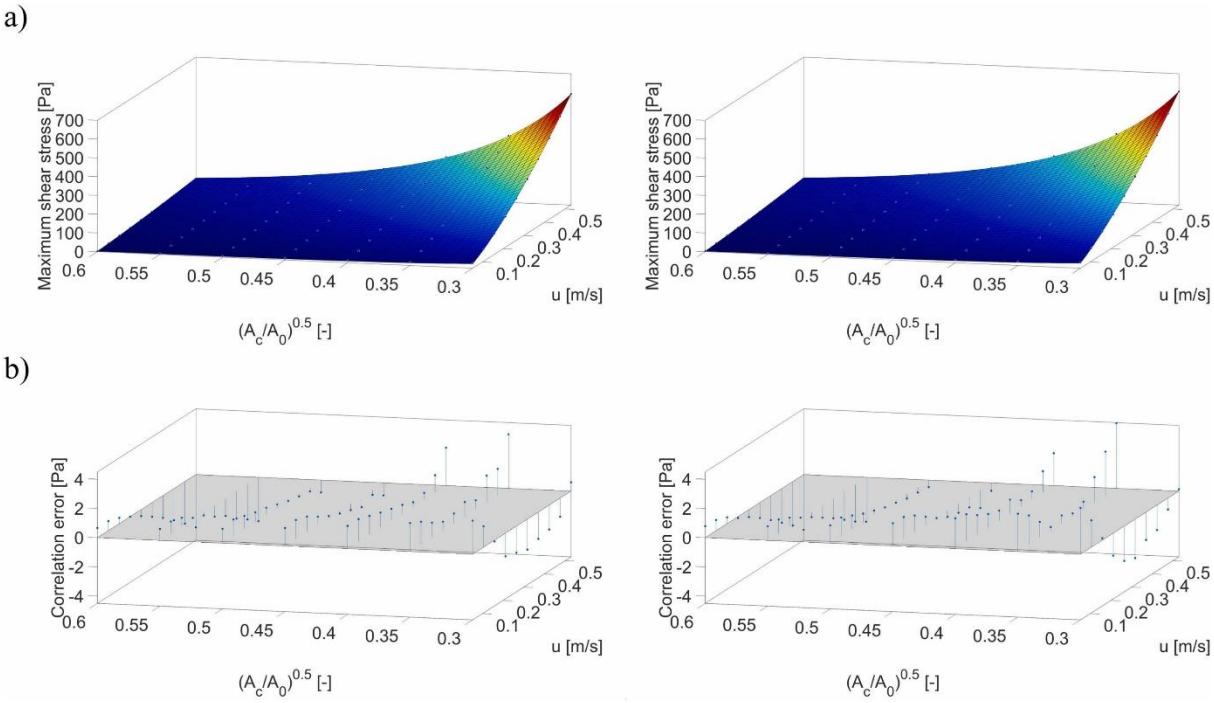

Figure 8. a) Maximum shear stress correlation vs. degree of stenosis and stenosis velocity for the Carreau–Yasuda (left) and population balance blood rheology (PBBR) (right) models. b) Maximum shear stress correlation error vs. degree of stenosis and stenosis velocity for the Carreau–Yasuda (L) and population balance blood rheology (PBBR) (R) models. [P3]

Figure 8 shows that as the flow velocity increases and the vessel lumen decreases, the maximum shear stress increases, which is associated with an increasing risk of hemolysis. The results obtained for the PBBR and Careau Yasuda viscosity models are consistent, and the obtained correlation has very similar parameters. The general correlation form is given by Eq. (52) [P3]

$$\tau_{max} = \alpha \cdot u^{\beta} \cdot \left[\left(\frac{A_c}{A_0}\right)^{0.5}\right]^{\gamma} \tag{52}$$

and Table 1 presents the correlation coefficients.

Table 1. The correlation (54) coefficients [P3].

Carreau–Yasuda blood model	PBBR model
$\alpha = 24.34$	$\alpha = 24.21$
$\beta = 1.398$	$\beta = 1.346$
$\gamma = -3.39$	$\gamma = -3.385$
with	with
$R^2 = 0.9999$	$R^2 = 0.9998$
$RMSE = 1.4243$	$RMSE = 1.6042$

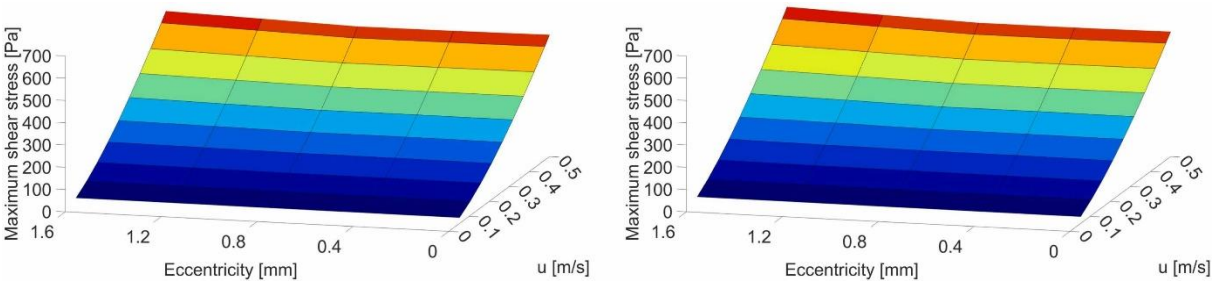

Figure 9. Correlation between maximum shear stress and the eccentricity of stenosis, as well as stenosis velocity, for the Carreau-Yasuda (L) and population balance blood rheology (PBBR) (R) models. [P3]

In the case of asymmetry of atherosclerotic narrowings, as seen in Figure 9, this effect is negligible.

In the next step, the influence of parameters such as the hydraulic diameter of the artery, the length and shape of the artery cross-section in the narrowing, which is associated with a change in its hydraulic diameter, was considered.

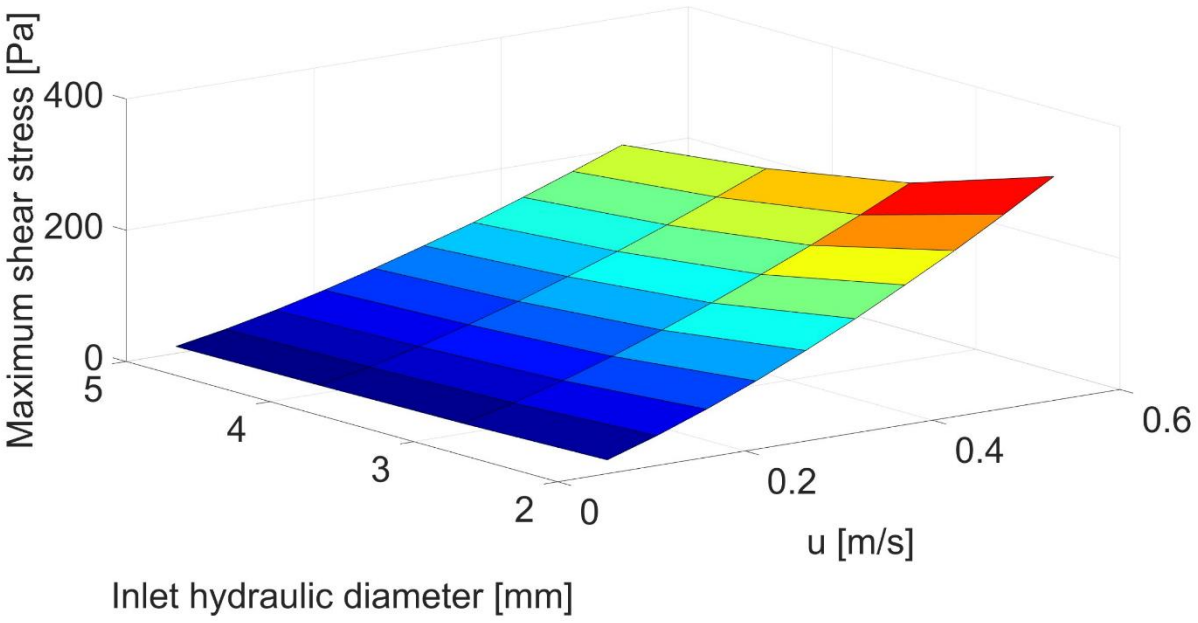

Figure 10. Correlation between inlet hydraulic diameter [mm] and mean velocity [m/s] for maximum shear stress. [P4]

In the case of the hydraulic diameter of the artery, it was observed that the smaller the diameter of the artery, the lower the flow speed at which hemolysis occurs, as can be seen in Figure 10.

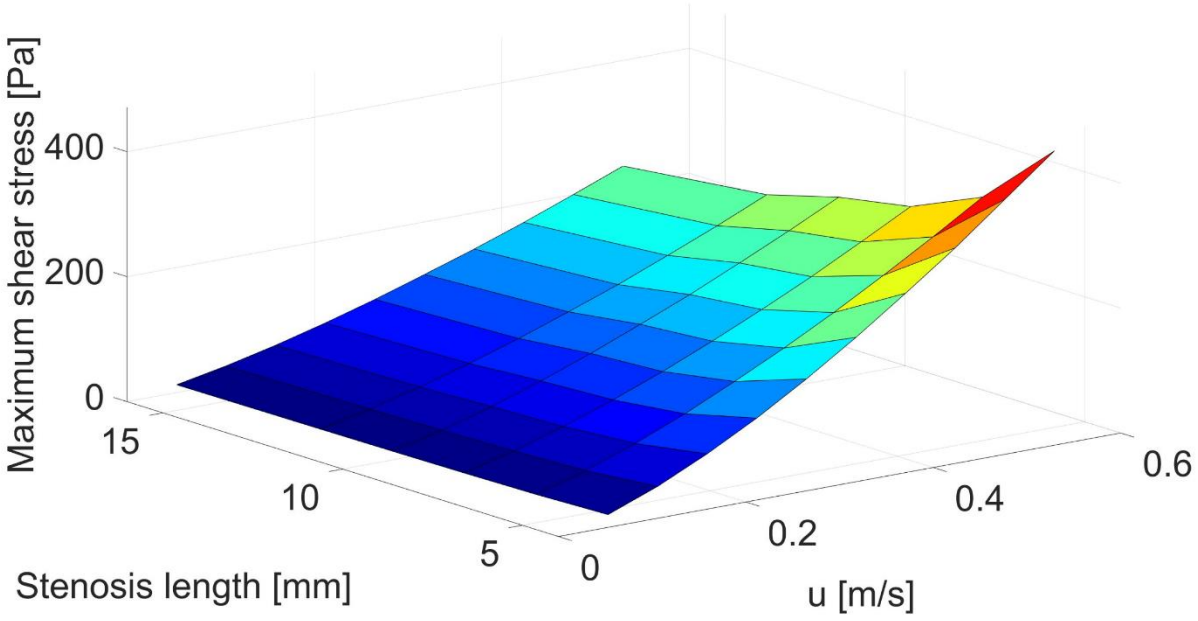

Figure 11. Correlation between stenosis length [mm] and mean velocity [m/s] for maximum shear stress. [P4]

Apparently, the relationship can be observed in Figure 11, the shorter the narrowing, the greater the increase in stress at the same light cross-sectional area at the narrowest point.

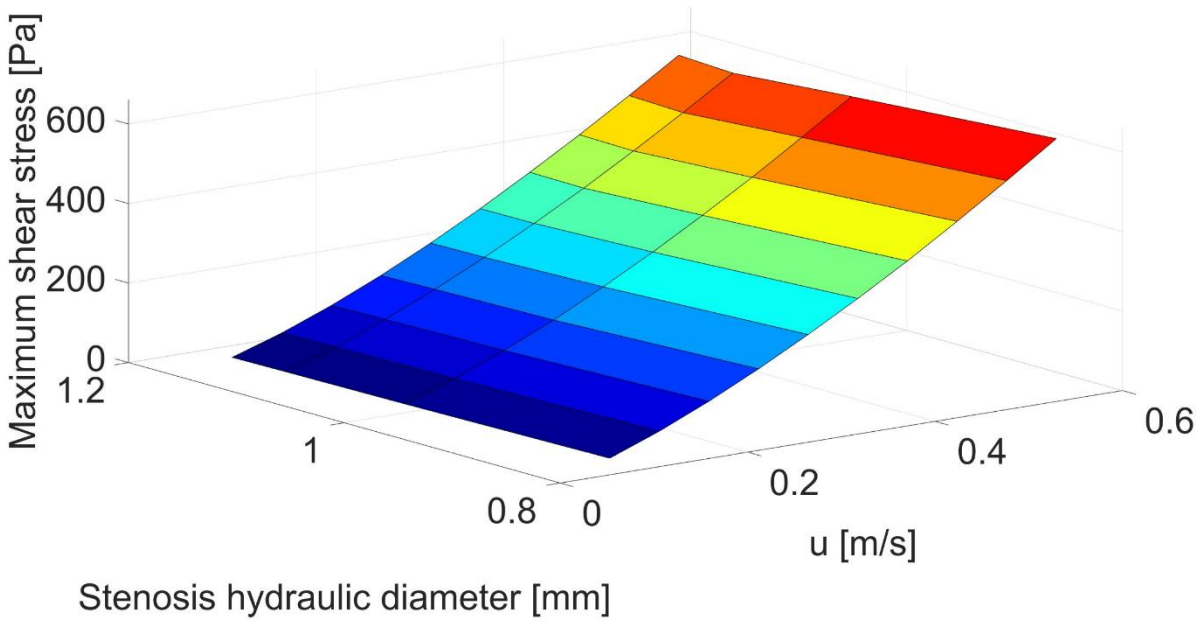

Figure 12. Correlation between stenosis hydraulic diameter [mm] and mean velocity [m/s] for maximum shear stress. [P4]

However, in the case of the shape of the necking itself, the relationship is still observable, but its significance is small, as can be seen in Figure 12.

6.3 Hypertension in atherosclerosis

The paper [P6] was prepared in collaboration with the Military Institute of Medicine—National Research Institute in Warsaw, the Medical University of Silesia in Katowice, and the University of Leeds (UK). Part of the work was prepared during a 3-month internship at the University of Leeds (UK), which began in September 2024, concluding the work for the doctoral thesis. In addition to mechanical hemolysis occurring in the case of severe atherosclerosis, the impact of atherosclerosis on the decrease in blood flow in vessels was analyzed, both without and with coexisting arterial hypertension. In order to properly model the phenomenon of blood flow reduction through the vessels of the left coronary artery, it was assumed that the static pressure at the inlet does not depend on the degree of narrowing but on whether the patient has hypertension or not. However, the resistance of distal fragments of arterial vessels depends only on the conditions of physical activity. A preview model of the boundary conditions is shown in Figure 13.

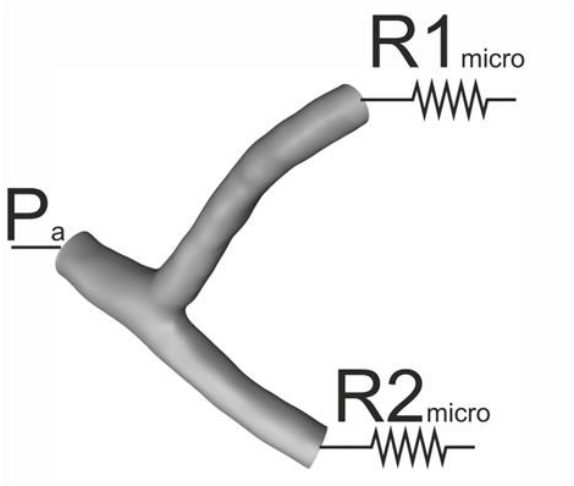

Figure 13. Boundary conditions schematic. [P6]

A series of simulations were performed for 4 variants of the boundary conditions of activity and arterial hypertension, and there were 7 models of constriction on vessel bifurcations plus a healthy artery as a reference.

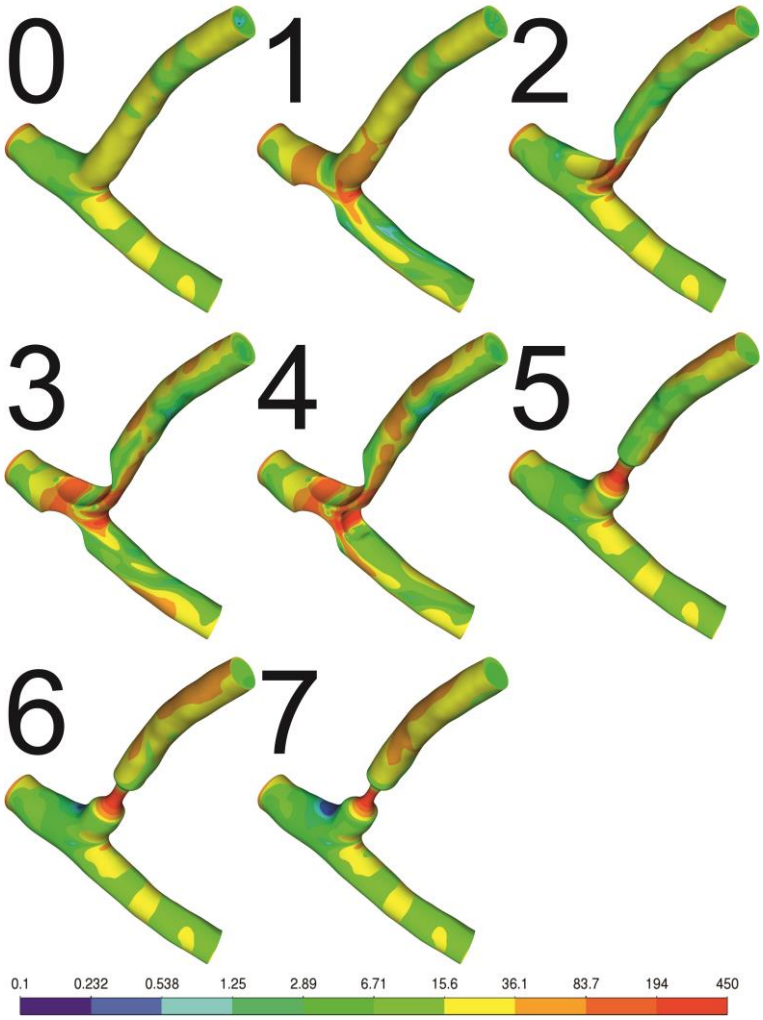

Figure 14. Contour plots of shear stress [Pa] for exercise without hypertension. [P6]

Figure 14 shows the results of wall shear stresses for physical activity conditions without excess pressure. As can be seen, in the case of severely narrowed vessels, the phenomenon of hemolysis is significant, while in the case of a healthy artery there is no such risk.

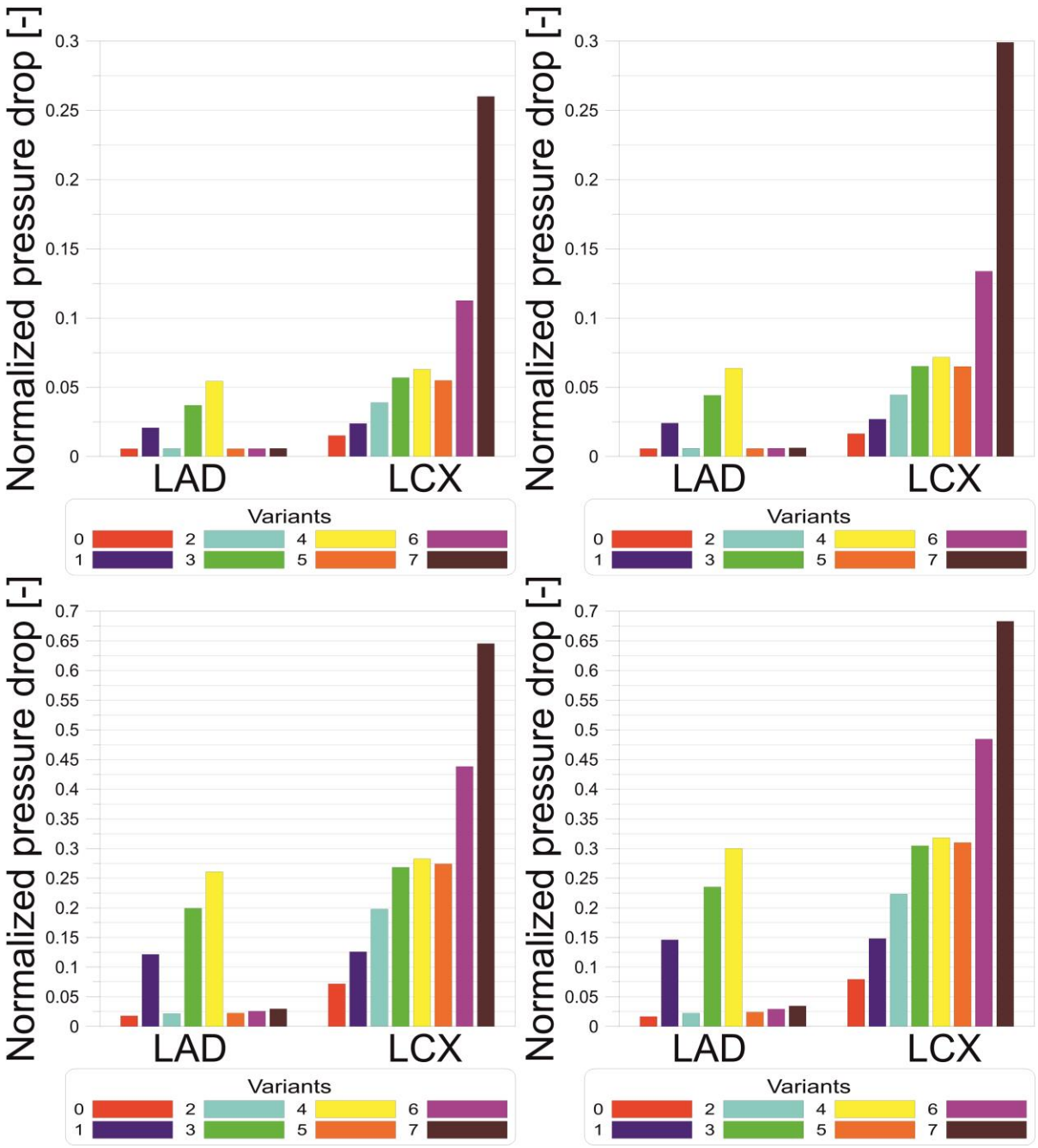

Figure 15. Normalized pressure [-] bar charts for (top left) rest without hypertension, (top right) rest with hypertension, (bottom left) exercise without hypertension, and (bottom right) exercise with hypertension. [P6]

Figure 15 shows the normalized pressure drop for all variants. As you can see, the effect of hypertension on the percentage pressure drop is almost imperceptible, but it can be seen that with a sudden increase in physical activity it increases rapidly. This relationship correlates with doctors' observations that many complications in people with atherosclerosis occur as a consequence of sudden physical exertion or physical trauma.

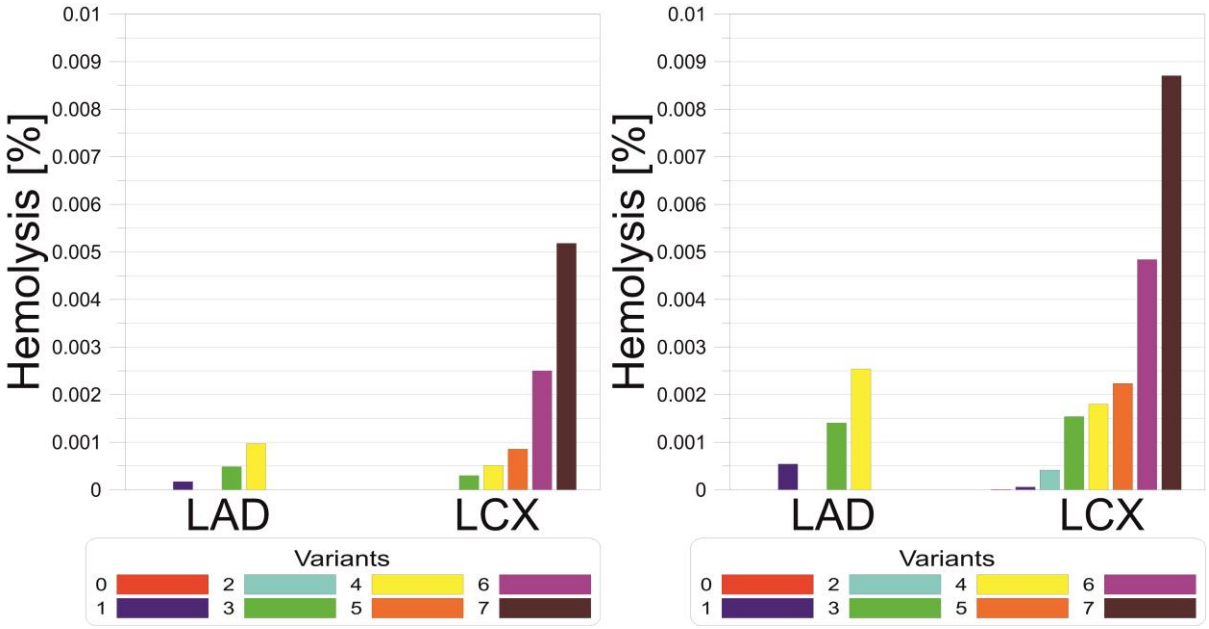

Figure 16. Hemolysis [%] bar charts for (left) exercise without hypertension and (right) exercise with hypertension. [P6]

However, Figure 16 shows that despite the lack of a significant impact on the level of blood flow in the arteries, coexisting arterial hypertension significantly increases the risk of hemolysis compared to atherosclerosis without coexisting hypertension.

7. Experimental analysis of blood flow

The experimental analysis of blood flow to verify the CFD simulations focused on 2D PIV experimental studies on models printed using Clear V4 resin from Formlabs on a Form 3B+ printer. In addition to preparing prints for measurements, the research included rheological measurements of solutions with a rheology similar to blood and analysis of their refractive index.

7.1 3D printing

3D models for 3D printing were divided into 2 categories: rigid prints for PIV tests made of Clear V4 resin and flexible prints for angioplasty tests made of Biomed Elastic 50A V1 resin.

3D models were prepared using CAD programs such as MeshMixer, ANSYS DesignModeler and ANSYS SpaceClaim. In the case of flexible models, the physiological thickness of the artery wall was taken into account. The prepared models were then exported in STL format to the PreForm program from Formlabs shown in Figure 17.

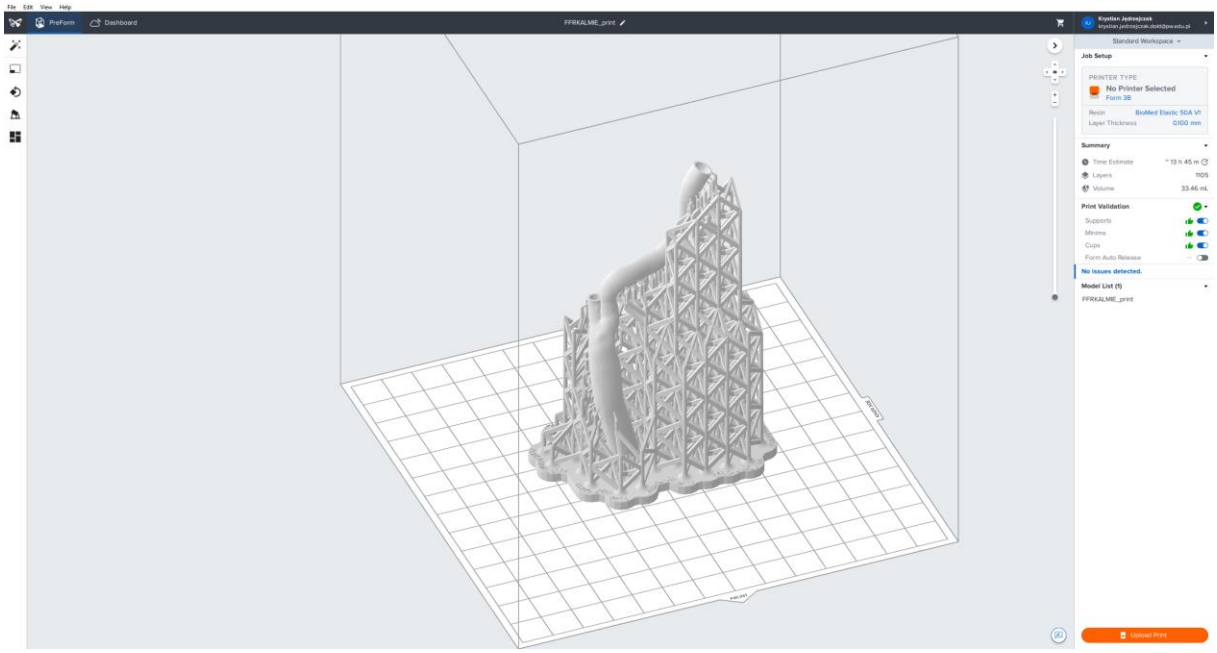

Figure 17. PreForm program window.

Printing parameters such as layer height and the number and type of supports were set in the PreForm program. With the update of the PreForm application, the ability to set your own print profiles related to accurate print calibration was also unlocked, which allowed for even greater print accuracy than reported in [P3], where accurate calibration functions were not yet available.

Figure 18. Biomed Elastic 50A V1 resin prints immersed in a beaker filled with water in Form Cure L.

After printing, it was necessary to wash the prints in isopropanol in the FormWash device in accordance with the manufacturer's recommendations. Then, the print had to be dried from the remains of isopropanol and subjected to a UV curing process in FormCure. In the case of the Clear V4 resin, the curing process takes place dry, while the Biomed Elastic 50A V1 resins should be performed wet in a beaker filled with distilled water as shown in Figure 18.

Using Clear V4 resin on the Form 3B+ printer, you can print very narrow channels of up to 0.5 mm in diameter, as can be seen in Figure 19, where you can see a test print of a cerebral artery with narrow branches.

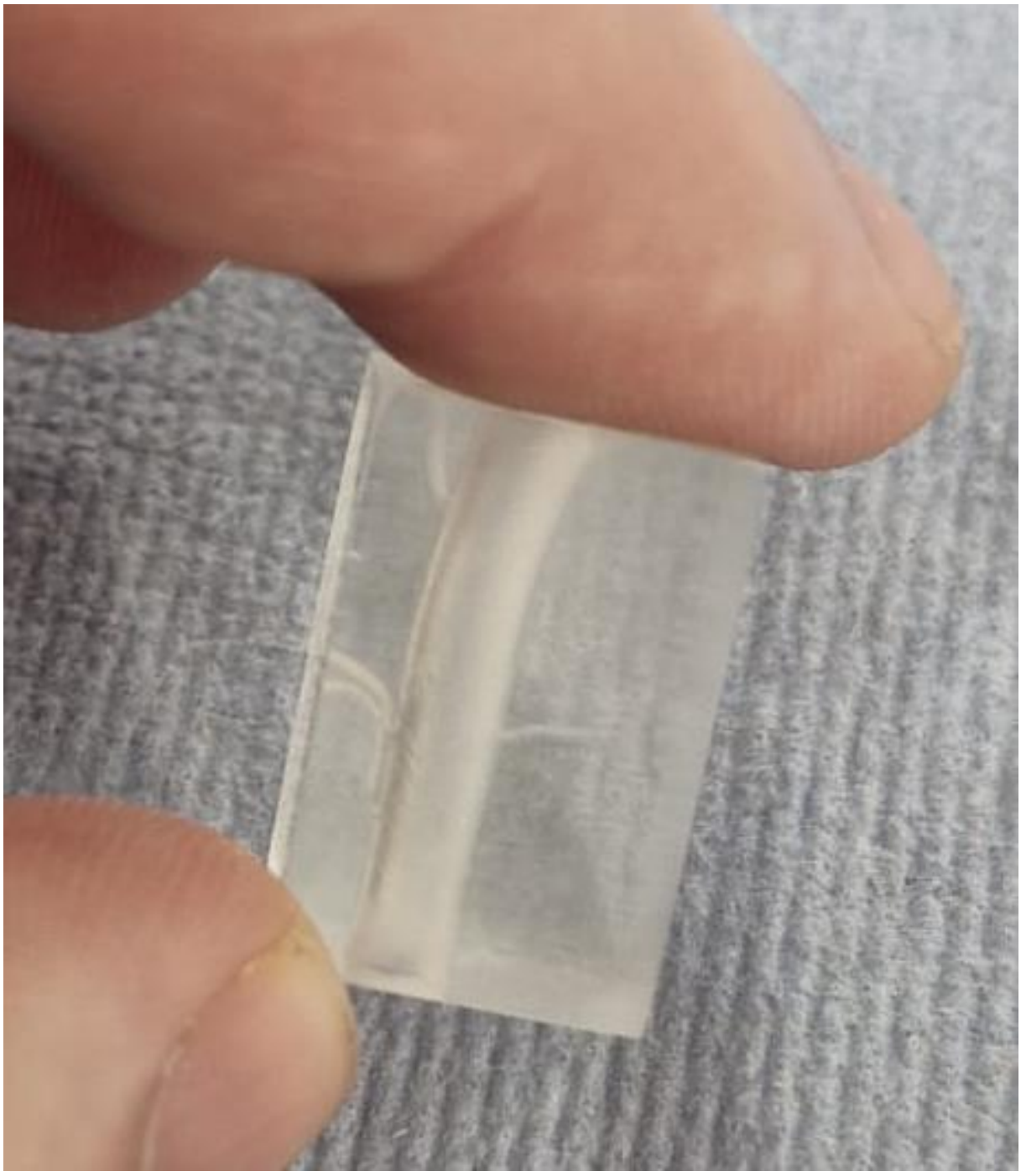

Figure 19. Preview print made of Clear V4 resin.

Models for PIV measurements were either very carefully polished on the laser and camera sides, or it is possible to use troughs to fill with a thin layer of solution to eliminate unevenness as shown in Figure 20.

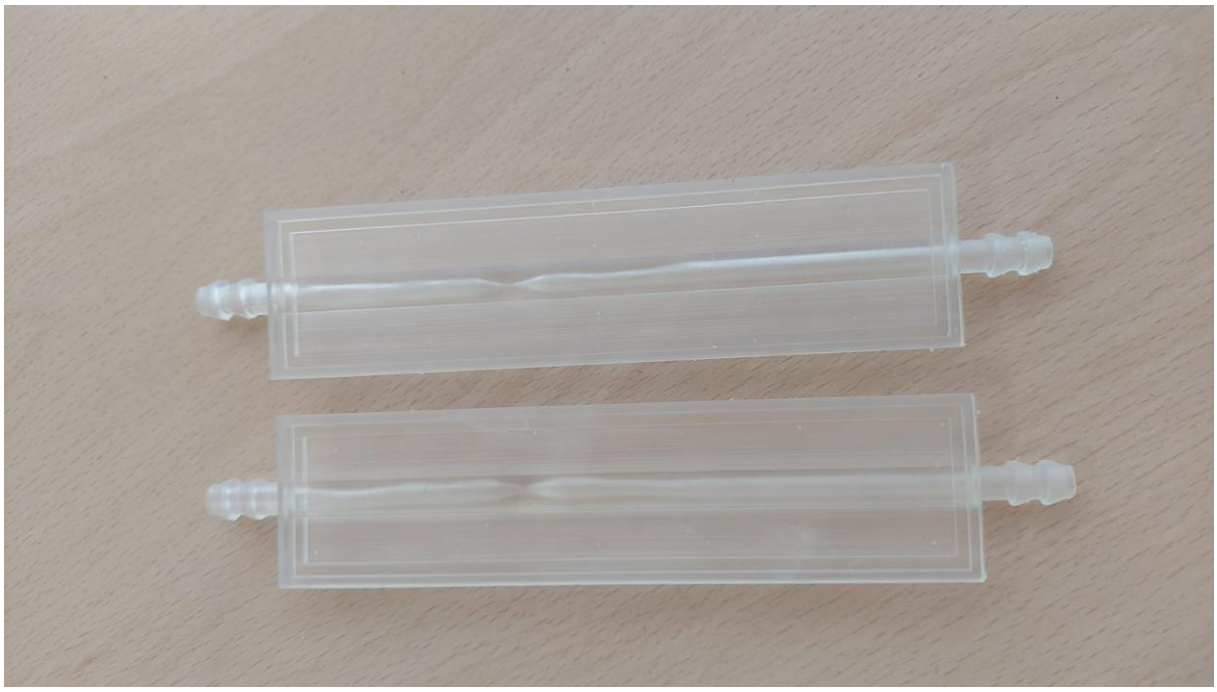

Figure 20. Clear V4 resin print for PIV measurements.

In the case of flexible models, a very important step was to skillfully remove the flexible supports so as not to damage the print, as can be seen in Figure 21.

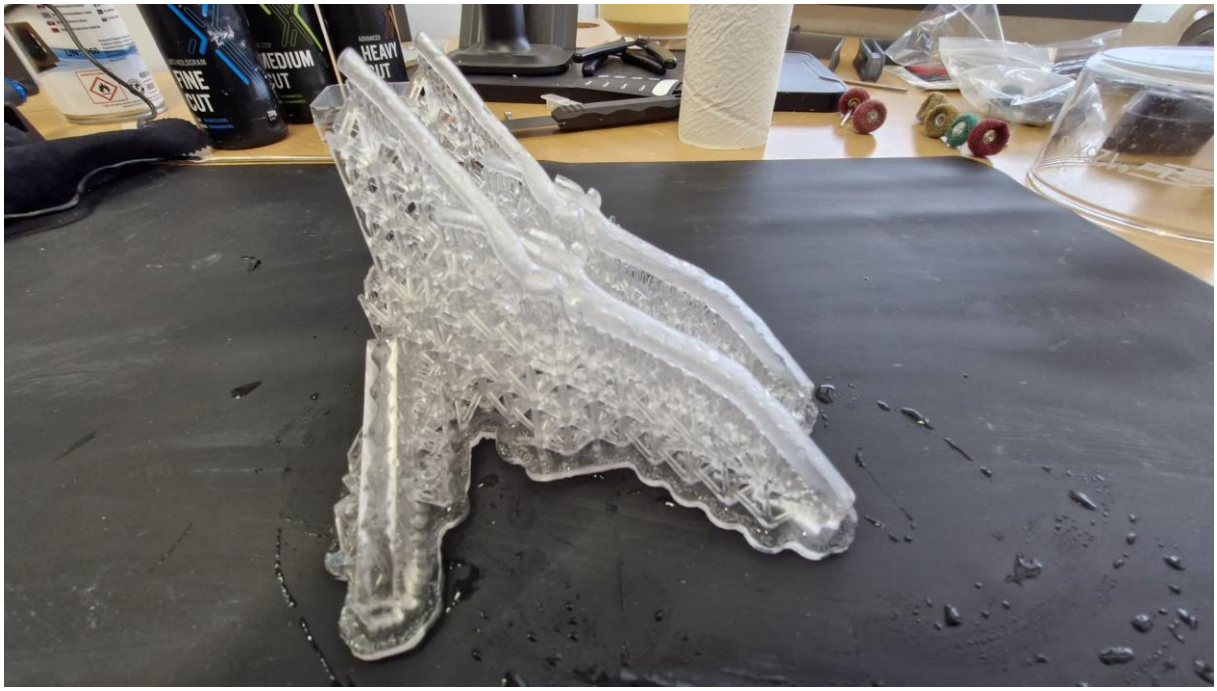

Figure 21. Biomed Elastic 50A V1 resin prints without supports removed.

Ready-made 3D models made of flexible resin are shown in Figure 22.

Figure 22. Prints made of Biomed Elastic 50A V1 resin after post-processing.

7.2 Rheology and refractive index matching experiments

The next stage of preparation for PIV measurements was to develop a liquid with a kinematic viscosity similar to blood and a refractive index the same as the Clear V4 resin print. In order to develop the solution, a series of measurements were made for various solutions, which were mixtures of water, glycerin, sodium iodide and sodium thiosulfate. Viscosity measurements were performed on an MCR 302 rheometer from Anton Parr. The density of the solutions was measured with a pycnometer. The refractive index measurements were made using a refractometer. The refractive index measurements were verified based on a system consisting of a calibration plate and a model with semicircular channels. In order to confirm the good fit of the refractive index, it was observed whether there was any refraction of light at the phase edge, as shown in Figure 23.

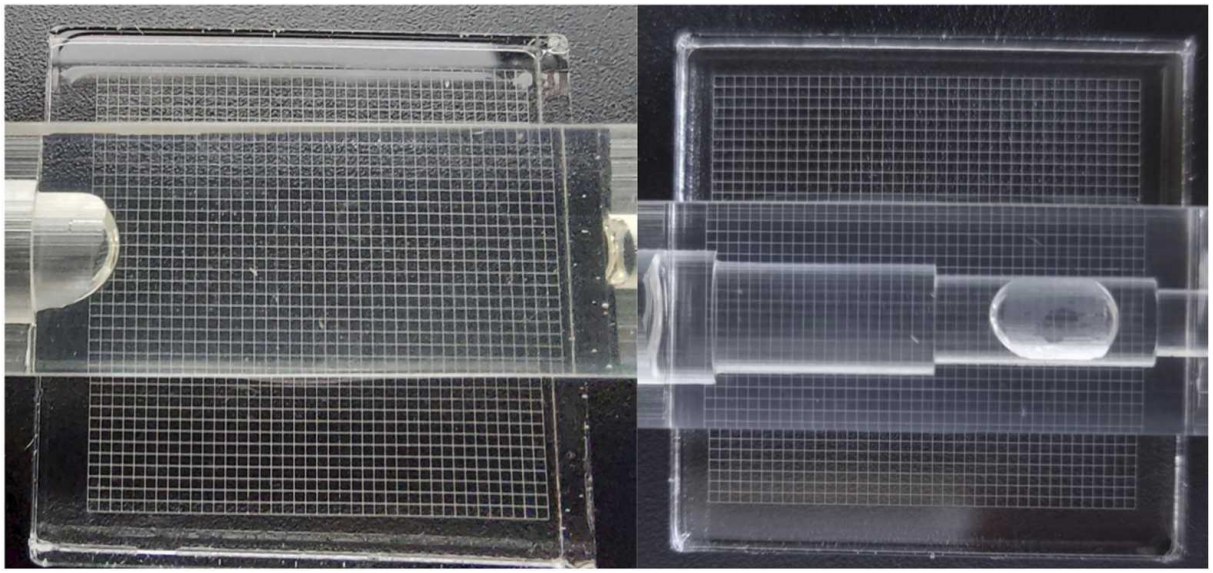

Figure 23. Calibration tools for refractive index matching; (left) µPIV fluid, (right) water. [P3]

7.3 Particle Image Velocimetry (PIV) as reference for CFD simulations

The system for PIV measurements is shown in Figure 24. It consisted of a laser light source, a syringe pump and a microscope with a connected camera, which allowed for the observation and recording of images from the sample.

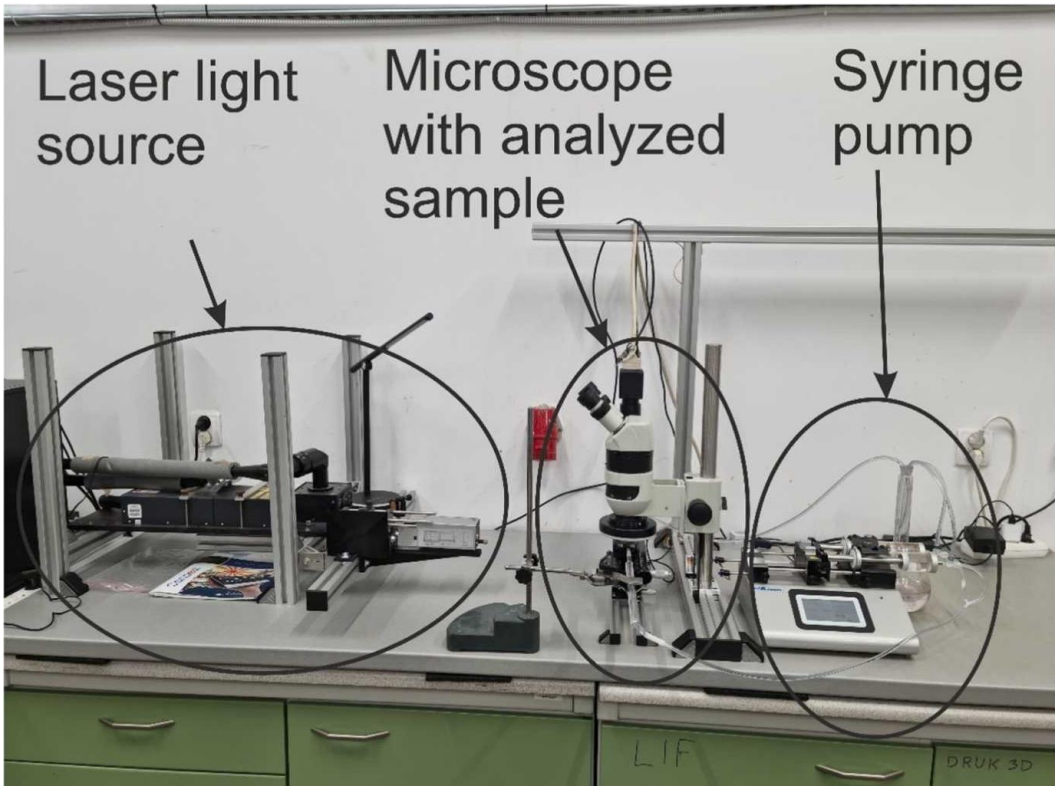

Figure 24. Measurement setup for micro-particle image velocimetry (µPIV). [P3]

A preview image of the tested geometry from seamlessly assembled photos is shown in Figure 25.

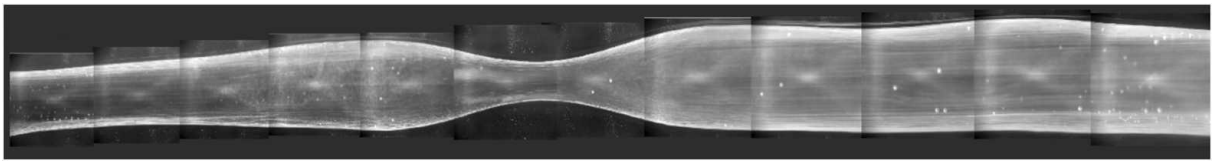

Figure 25. 3D artery phantom (the picture was acquired of the phantom filled with water to capture the walls). [P3]

Figure 26 shows the comparison of CFD and PIV results for two flow rates. As you can see, the simulation and experiment results are similar. CFD simulation is able to predict stagnation and recirculation zones and the shape of the jet behind the choke, which proves the correctness of the numerical analysis.

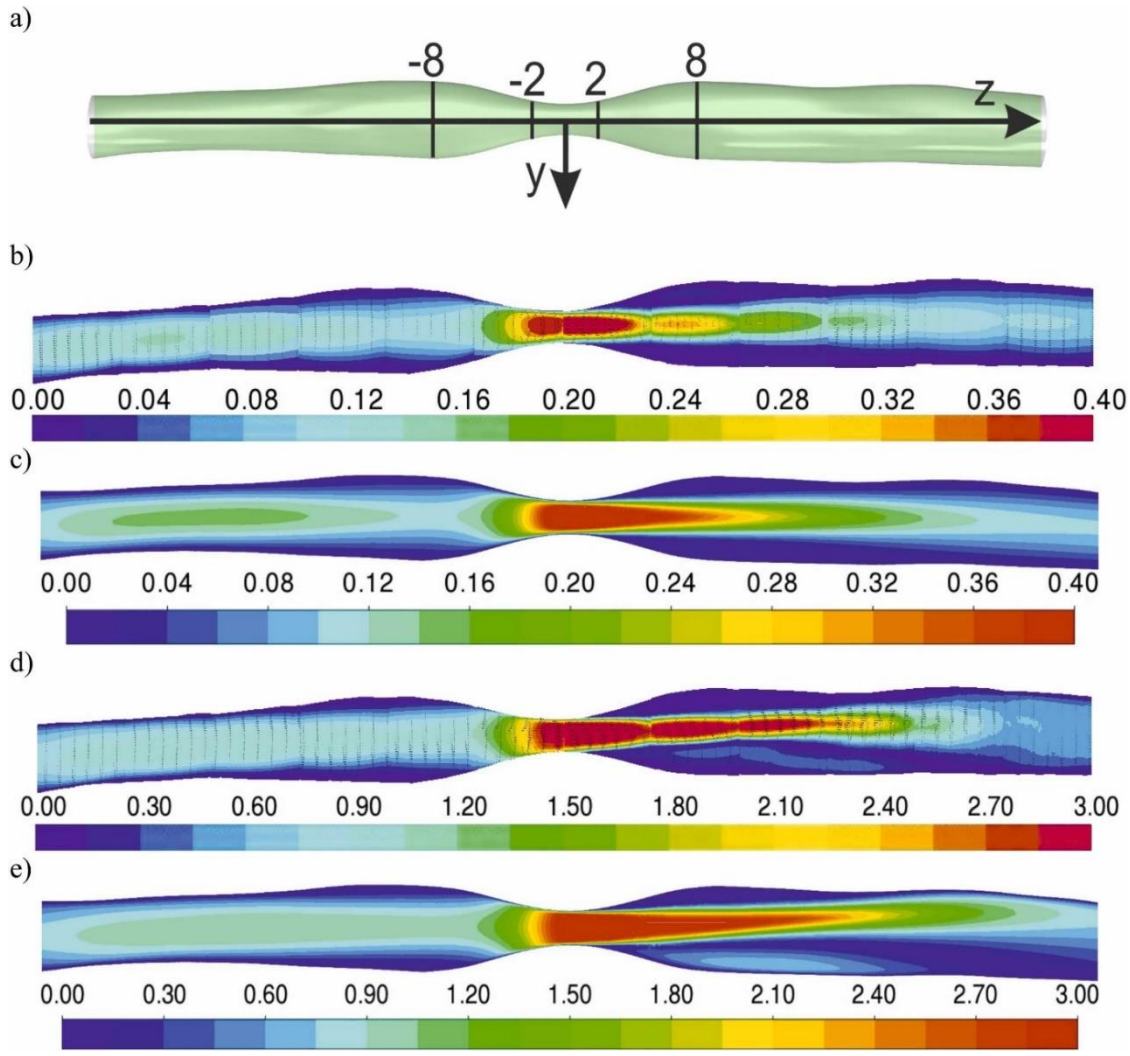

Figure 26. a) 3D model with cross-sections for velocity profile comparison. The green cross-section is used for μPIV measurements and computational fluid dynamics comparison.

b) Contours of a velocity magnitude obtained from μPIV measurements for a flow rate of 0.625 mL/s. c) Contours of a velocity magnitude obtained from computational fluid dynamics simulation for a flow rate of 0.625 mL/s. d) Contours illustrating velocity magnitude obtained from μPIV measurements at a flow rate of 5 mL/s. e) Contours illustrating velocity magnitude obtained from computational fluid dynamics simulation at a flow rate of 5 mL/s. [P3]

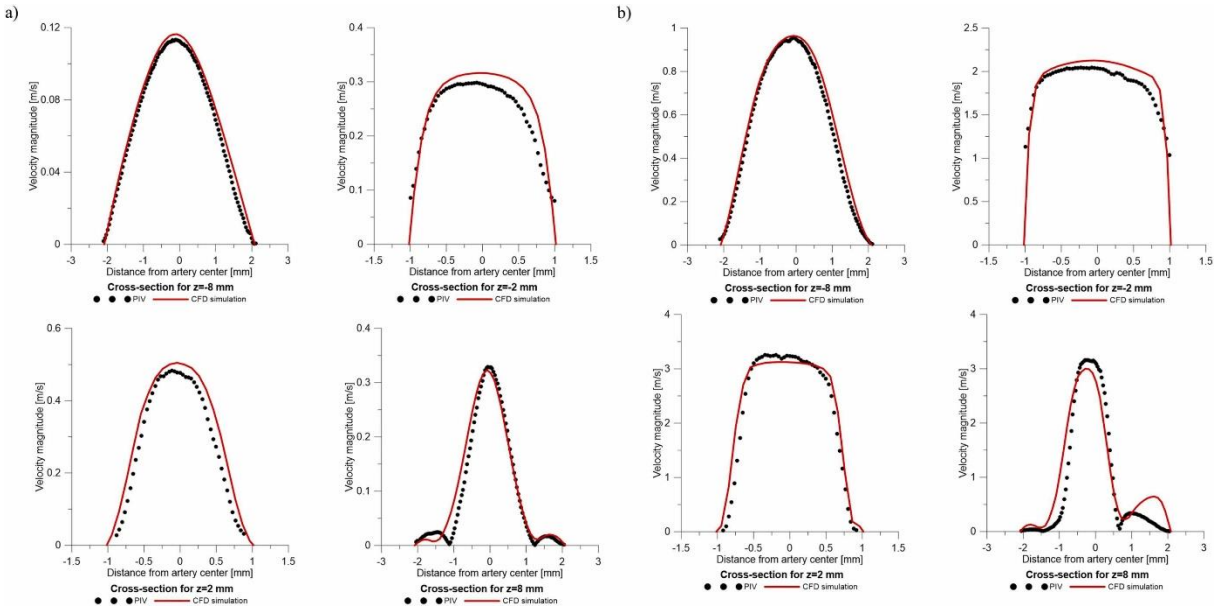

Figure 27. Comparison of μPIV measurements and CFD simulation at two different flow rates: a) 0.625 mL/s b) 5 mL/s. [P4]

In order to more precisely analyze the correctness of the CFD simulation, velocity profiles for the cross-sections from Figure 26a are presented in Figure 27. As can be seen, there is a very high consistency between the results, which proves the high accuracy of the print and the correctness of the CFD simulation. Moreover, it is worth mentioning that the high agreement of experimental results obtained would not have been possible without the appropriate liquid simulating blood rheology, which, apart from the appropriate kinematic viscosity parameters, had a refractive index identical to the refractive index of the material from which the arterial model was made. The paper [71] presents the influence of the change in the refractive index on the correctness of the measurement, where the fact of adding glycerin to water, reducing the differences between the refractive indices of light, has a positive effect on the correctness of the obtained data. As part of the presented paper [P4], the addition of sodium iodide allowed for the complete elimination of the difference in the refractive index, which was verified experimentally based on the measurement of light refraction using a refractometer, and based

on the system with a calibration plate, which was filled with the working fluid, where the fact of light refraction on the inner wall of the model was observed as presented in paper [P4].

8. Methods of treating atherosclerosis

Treatment of atherosclerosis is divided into pharmacological and surgical interventions. Pharmacological treatment most often involves inhibiting or reducing the production of cholesterol, especially LDL [108–111]. However, in the case of surgical interventions, treatments such as: Angioplasty and stent placement [112, 113], Endarterectomy [114], Fibrinolytic therapy [115] or Coronary artery bypass graft (CABG) surgery [116].

8.1 Angioplasty with stent placement

Angioplasty is a medical procedure used to open narrowed or blocked blood vessels, often performed alongside stent placement [112, 113]. Before the procedure begins, patients may be given pain relievers, sedatives, and blood-thinning medications to prevent clot formation. During the procedure, the patient lies down, remaining conscious, while the doctor inserts a flexible tube called a catheter into an artery. The entry point is usually in the groin area, though it may vary depending on the location of the blockage. Using live X-ray imaging, the doctor carefully guides the catheter through the arteries toward the heart. A liquid contrast agent, sometimes referred to as "dye," is injected to highlight blood flow through the arteries, allowing the doctor to identify the areas of narrowing. Once the blockage is located, a guide wire is threaded through the narrowed segment of the artery, and a balloon catheter is advanced over the wire to the site of the blockage. The balloon is then inflated, which expands the artery and restores normal blood flow. In many cases, a stent is then placed at the site of the blockage to help keep the artery open. The stent is delivered along with the balloon catheter and expands as the balloon inflates. After the stent is in place, the balloon is deflated and removed, while the stent remains in the artery to ensure it stays open.

8.2 Low-cost angioplasty practice station

The article [P5] was prepared in cooperation with the Military Institute of Medicine—National Research Institute in Warsaw, who was responsible for the substantive support from the medical side and performed simulated angioplasty procedures on 3D printed phantoms, ensuring the correctness of the simulated medical procedure. Due to the possibility of complications after angioplasty, especially in the case of complex procedures where there is a high risk of damage to the atherosclerotic plaque, which may block distal parts of the circulatory system, blocking oxygenation of the heart muscle or brain, there is a need for appropriate

planning of the procedure and training of interventional radiologists and cardiac surgeons. This is where 3D printing comes in handy. Combined with non-invasive imaging methods, it allows you to print flexible models of arteries, which are ideal training material for doctors to minimize the risk of post-operative complications.

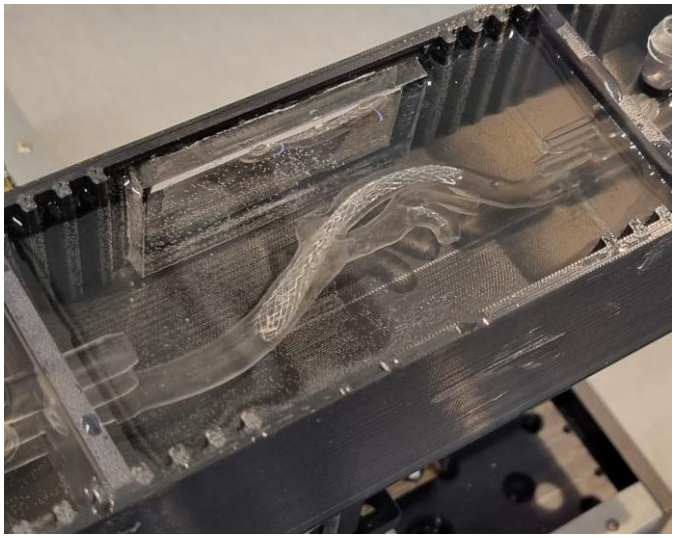

Figure 28. Experimental setup for percutaneous carotid artery stenting procedure. [P5]

Figure 28 shows the proposed system for angioplasty training, which consists of a 3D printed model made of Biomed Elastic 50A V1 resin and a glycerin container printed on an FFF printer, because the refractive index of the print is very close to the refractive index of pure glycerin, which allows obtaining very good image quality using cheap and non-toxic liquid. The system can be extended with an image acquisition camera, allowing for convenient training with the ability to record images for later analysis. Samples of prints made of Biomed Elastic 50A V1 resin were tested on an Instron testing machine, the measured Young's modulus was 2.2 MPa, which is a value similar to the strength parameters of natural arteries. The developed system not only allows for training doctors and planning procedures, but is also a good tool for comparing different types of stents in the same case, as shown in Figure 29 and 31.

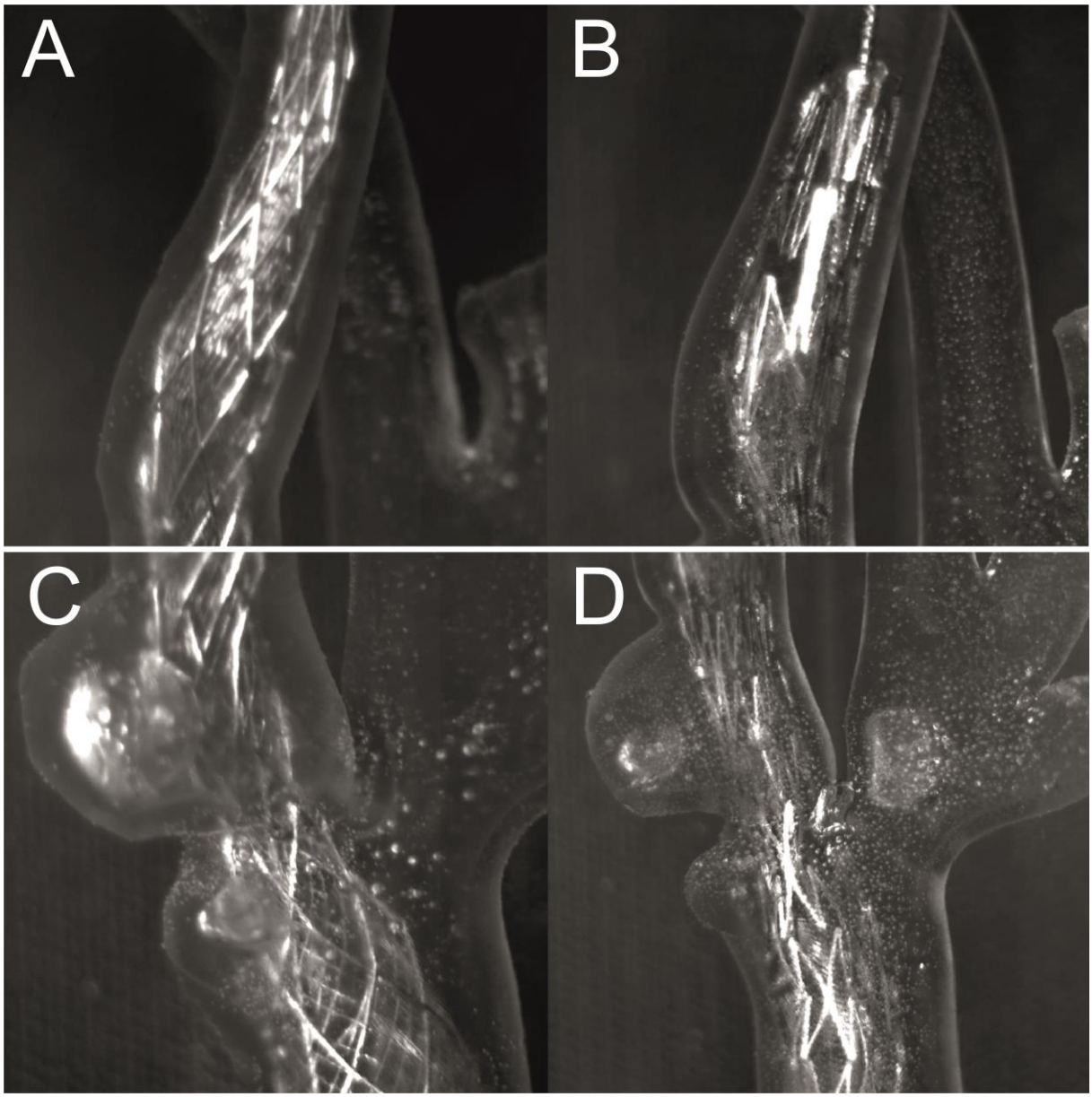

Figure 29. Comparison of stents for two exposures, A and C - dense mesh (Roadsaver™ - Carotid Artery Stent), B and D - sparse mesh (Protégé™ RX - Carotid Artery Stent). [P6]

In Figure 29, we can see a different way of adjusting the stent to the model wall depending on the mesh density.

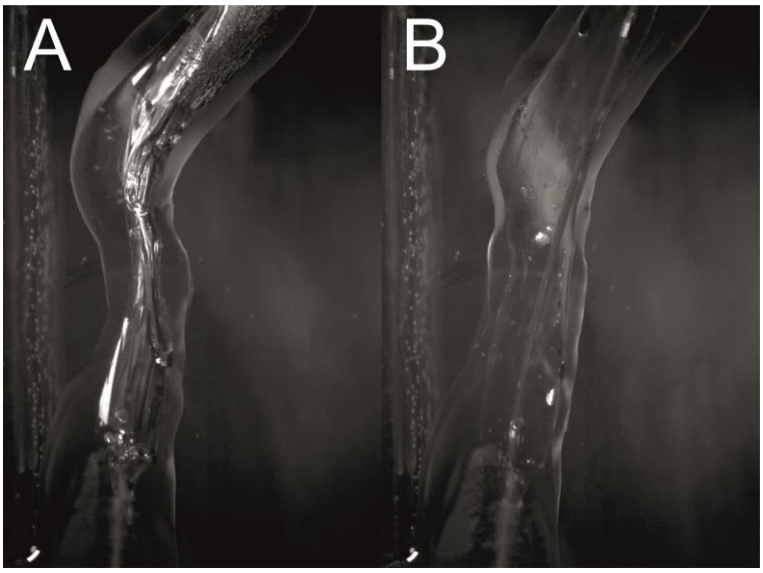

Figure 30. Comparison of artery model before (A) and after (B) inflating the balloon.

Moreover, it is also possible to observe the expansion of the vessel lumen under the influence of the balloon, as shown in Figure 30.

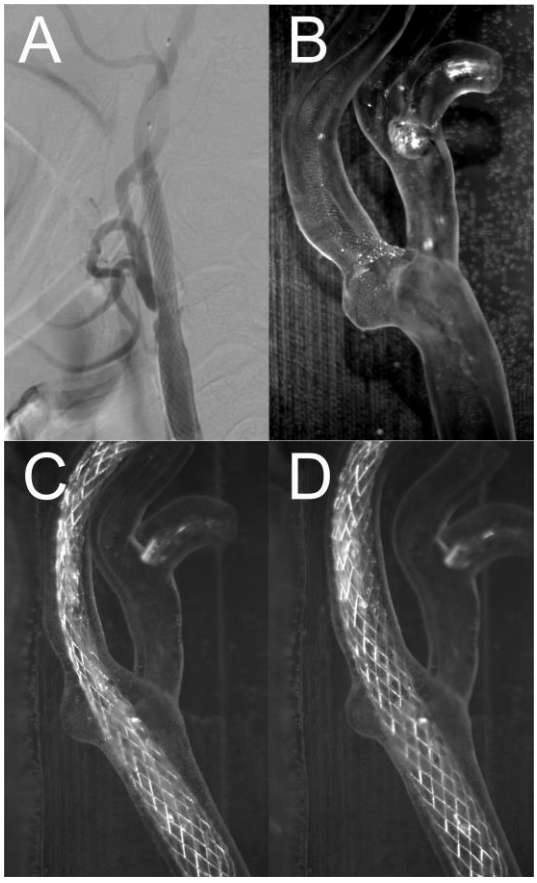

Figure 31. Comparison of artery with Carotid WALLSTENT™ after angioplasty with stent placement (A) and carotid artery model (B) with carotid artery stent before (C) and after (D) inflating the balloon.

The obtained results are consistent with the results of the treatments, which can be seen in the comparison with the patient in Figure 31.

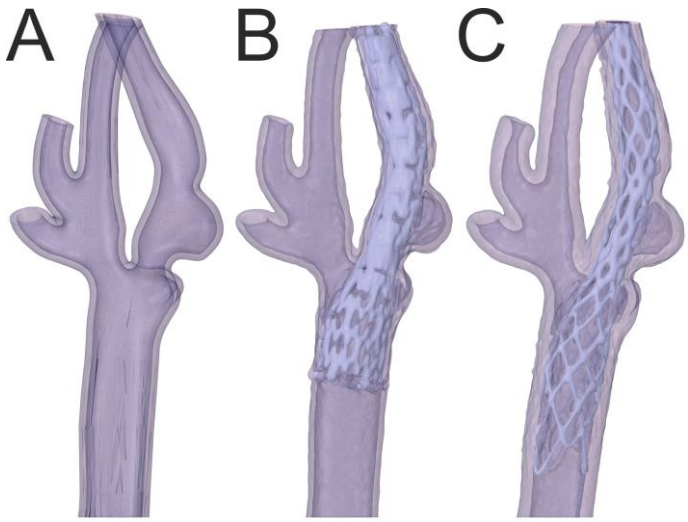

Figure 32. Comparison of CT images: (A) geometry without stent, (B) with Roadsaver™ - Carotid Artery Stent, (C) with Protégé™ RX - Carotid Artery Stent.

Figures 32 and 33 show a comparison of different stents and base models using cone beam computed tomography. As can be seen by comparing Figures 33 and 34 with Figures 30 and 32, the optical resolution of the camera is higher than in the case of classic medical imaging methods. To improve the resolution of the analysis, the use of a microCT device is required.

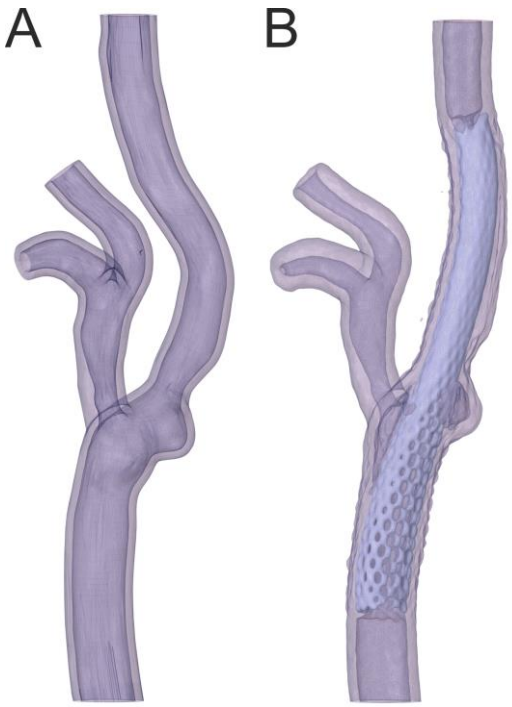

Figure 33. Comparison of CT images: (A) geometry without stent, (B) with Carotid WALLSTENT™.

9. Conclusions

The doctoral thesis aims to develop a correlation between the risk of hemolysis associated with the maximum shear stress and the hydrodynamic and geometric parameters of the artery, verified using experimental fluid mechanics with 3D printed phantoms. An additional goal is to create a universal and economical workshop for training in angioplasty using 3D printing devices and experimental fluid mechanics, which can be easily adapted to the training of medical students and to prepare for procedures with a potentially high risk of postoperative complications. In order to achieve the intended objectives of the dissertation, advanced computational and experimental techniques such as computational fluid dynamics (CFD), 3D printing, and experimental fluid mechanics were explored, which can be applied to improve the diagnosis and treatment planning of atherosclerosis and related conditions such as hypertension. These diseases are significant health concerns, and their treatment often involves complex decision-making processes, particularly when it comes to evaluating blood flow dynamics in stenotic arteries caused by plaque buildup. The work leverages modern technological advancements, especially in medical imaging and 3D modeling, to improve the accuracy and predictive capabilities in medical scenarios. A key focus of the thesis is the growing use of computational fluid dynamics (CFD) and 3D printing in medical applications. These technologies are increasingly adopted due to the rapid development of computer processing power and 3D printing technologies. As CFD becomes more advanced, it can model complex biological flows, while 3D printing allows for the physical creation of anatomically accurate models based on high-resolution medical imaging. This makes the approach especially valuable for analyzing diseases like atherosclerosis, where blood flow characteristics are central to diagnosis and treatment. Moreover, the thesis highlights how the improvement of medical imaging technologies; including computed tomography (CT) and magnetic resonance imaging (MRI), specifically 4D flow MRI; provides detailed insights into the blood flow fields within vessels [T1]. These advancements enable the creation of highly accurate 3D models of arteries and surrounding tissues, which can be used both for simulation and 3D printing. The integration of these technologies offers a non-invasive means of predicting patient-specific risk factors and guiding surgical interventions.

An essential part of the thesis involves studying the influence of geometric parameters on hemolysis, a condition where red blood cells (RBCs) are destroyed, leading to complications. Hemolysis is one of the common risks associated with advanced atherosclerosis. To understand this risk, a novel blood rheology model based on population balance was developed, accounting

for the hemolysis of individual RBCs [P1]. This model goes beyond traditional representations of blood flow, simulating the agglomeration and deaglomeration of RBCs, capturing the thixotropic behavior of blood; a non-Newtonian property that explains how blood viscosity changes under stress. The simulations conducted using the ANSYS Fluent environment revealed key insights. The maximum shear stress during steady-state flow emerged as a critical risk factor for hemolysis. This was further verified in time-averaged wall shear stress (TAWSS) studies, which showed a near-identical correlation between TAWSS over a cardiac cycle and shear stress during the average steady-state flow. These findings were detailed in Article [P2]. In paper [P3], it was shown how increasing the degree of arterial stenosis raises the risk of hemolysis, using both the PBBR and Carreau-Yasuda models, yielding consistent results. Additionally, it was shown that the degree of eccentricity of coronary stenosis does not significantly impact the increased risk of hemolysis. Meanwhile, in article [P4], the analysis was extended to generalize the relationships to variable stenosis lengths, the hydraulic diameter of the coronary vessel, and the stenosis. The obtained relationships confirm the hypothesis presented in [T2].

The obtained relationships required appropriate experimental verification. For this purpose, suitable coronary artery phantoms were necessary, related to hypothesis [T3]. In works [P3, P5], the 3D printing technology of transparent artery models, both rigid [P3] and flexible [P5], was presented. The SLA-LFS technology used allowed for a high level of transparency in the models and high print resolution. Based on the obtained 3D artery models, μPIV measurements were possible to verify the accuracy of computer simulations in ANSYS Fluent software. In paper [P3], a comprehensive comparison of CFD simulation results and experimental flow measurements was presented, using the μPIV technique, where blood was replaced with a liquid that had the same kinematic viscosity and refractive index as the 3D-printed model to eliminate image distortion due to light refraction at the phase boundary. The agreement of the results confirmed hypothesis [T4].

In the next phase, the focus shifted to the mechanical and optical properties of the flexible resin Biomed Elastic 50A V1, which was found to closely resemble the mechanical properties of arterial walls. This similarity confirmed hypothesis [T5] and was presented in Article [P5]. This material's combination of strength and flexibility, along with its low refractive index compared to other resins like Clear V4, made it ideal for developing a cost-effective and easy-to-use training setup for angioplasty with stent placement procedures. The training setup was tested in collaboration with the Military Institute of Medicine, and the results

were published in Article [P5]. The setup offered a practical tool for interventional radiologists and surgeons, providing a realistic model for preoperative training, particularly valuable for procedures involving stent implantation, where precise handling is critical.

The final phase of the thesis extended the analysis of atherosclerotic complications by incorporating the influence of hypertension, particularly in the bifurcation of the left coronary artery. This extension was closely related to hypothesis [T2] and examined how hypertension interacts with atherosclerotic stenosis beyond its geometric shape. The study, presented in Article [P6], demonstrated that hypertension significantly increases the risk of hemolysis compared to patients without hypertension. This finding is especially relevant in clinical settings where both conditions frequently coexist.

In conclusion, this thesis provides a thorough investigation into the factors influencing hemolysis in atherosclerosis patients, offering valuable insights for clinicians to improve the diagnosis and management of atherosclerosis-related complications. The research combined CFD simulations, experimental validations, and 3D printing technologies to establish a robust framework for understanding blood flow dynamics in diseased arteries. Additionally, the development of a low-cost preoperative training system for angioplasty with stent placement is a notable contribution, offering a practical tool for improving surgical outcomes. Overall, this work demonstrates the potential of integrating advanced computational models with experimental techniques to enhance patient care in cardiovascular medicine.

List of Figures

List of Tables

References

1. Alpert JS (2012) A few unpleasant facts about atherosclerotic arterial disease in the United States and the world. American Journal of Medicine 125:839–840
2. Amini M, Zayeri F, Salehi M (2021) Trend analysis of cardiovascular disease mortality, incidence, and mortality-to-incidence ratio: results from global burden of disease study 2017. BMC Public Health 21:. https://doi.org/10.1186/s12889-021-10429-0
3. Kim H, Kim S, Han S, Rane PP, Fox KM, Qian Y, Suh HS (2019) Prevalence and incidence of atherosclerotic cardiovascular disease and its risk factors in Korea: A nationwide population-based study. BMC Public Health 19:. https://doi.org/10.1186/s12889-019-7439-0
4. (2024) https://ec.europa.eu/eurostat/web/products-eurostat-news/-/edn-20200928-1
5. Henning RJ (2021) Obesity and obesity-induced inflammatory disease contribute to atherosclerosis: a review of the pathophysiology and treatment of obesity
6. Spector R (2016) New insight into the dietary cause of atherosclerosis: Implications for Pharmacology. Journal of Pharmacology and Experimental Therapeutics 358:103–108
7. Giersiepen M, Wurzinger LJ, Opitz R, Reul H (1990) Estimation of shear stress-related blood damage in heart valve prostheses-in vitro comparison of 25 aortic valves. Int J Artif Organs 13:300–306
8. Lacasse D, Garon A, Pelletier D (2007) Mechanical hemolysis in blood flow: user-independent predictions with the solution of a partial differential equation. Comput Methods Biomech Biomed Engin 10:1–12
9. Michel JB, Martin-Ventura JL (2020) Red blood cells and hemoglobin in human atherosclerosis and related arterial diseases. Int J Mol Sci 21:1–20
10. Li Q, Ding Y, Chen Q, Tang Y, Zhang H, He Y, Fu G, Yang Q, Shou X, Ye Y, Zhao X, Zhang Y, Li Y, Zhang X, Wu C, Wang R, Xu L, Zhang R, Yeung A, Zeng Y, Qian X (2023) Diagnostic Performance of a Novel Automated CT-derived FFR Technology in Detecting Hemodynamically Significant Coronary

Artery Stenoses: A Multicenter Trial in China. Am Heart J. https://doi.org/10.1016/j.ahj.2023.08.009

11. Stary HC, Chandler AB, Dinsmore RE, Fuster V, Glagov S, Insull W, Rosenfeld ME, Schwartz CJ, Wagner WD, Wissler RW (1995) A Definition of Advanced Types of Atherosclerotic Lesions and a Histological Classification of Atherosclerosis . Circulation 92:1355–1374. https://doi.org/10.1161/01.CIR.92.5.1355

12. Virmani R, Kolodgie FD, Burke AP, Farb A, Schwartz SM (2000) Lessons From Sudden Coronary Death . Arterioscler Thromb Vasc Biol 20:1262–1275. https://doi.org/10.1161/01.ATV.20.5.1262

13. van Veelen A, van der Sangen NMR, Henriques JPS, Claessen BEPM (2022) Identification and treatment of the vulnerable coronary plaque. Rev Cardiovasc Med 23

14. Nakazawa G, Yazdani SK, Finn A V., Vorpahl M, Kolodgie FD, Virmani R (2010) Pathological Findings at Bifurcation Lesions: The Impact of Flow Distribution on Atherosclerosis and Arterial Healing After Stent Implantation. J Am Coll Cardiol 55:1679–1687. https://doi.org/10.1016/J.JACC.2010.01.021

15. Thiagarajan P, Parker CJ, Prchal JT (2021) How Do Red Blood Cells Die? Front Physiol 12

16. Wojtas K, Kozłowski M, Orciuch W, Makowski Ł (2021) Computational Fluid Dynamics Simulations of Mitral Paravalvular Leaks in Human Heart. Materials 14:. https://doi.org/10.3390/ma14237354

17. Kozłowski M, Wojtas K, Orciuch W, Smolka G, Wojakowski W, Makowski Ł (2022) Parameters of Flow through Paravalvular Leak Channels from Computational Fluid Dynamics Simulations-Data from Real-Life Cases and Comparison with a Simplified Model. J Clin Med 11:. https://doi.org/10.3390/jcm11185355

18. Kozłowski M, Wojtas K, Orciuch W, Jędrzejek M, Smolka G, Wojakowski W, Makowski Ł (2021) Potential Applications of Computational Fluid Dynamics for Predicting Hemolysis in Mitral Paravalvular Leaks. J Clin Med 10:. https://doi.org/10.3390/jcm10245752

19. Garon A, Farinas M-I (2004) Fast Three-dimensional Numerical Hemolysis Approximation. Artif Organs 28:1016–1025. https://doi.org/https://doi.org/10.1111/j.1525-1594.2004.00026.x

20. Arvand A, Hormes M, Reul H (2005) A validated computational fluid dynamics model to estimate hemolysis in a rotary blood pump. Artif Organs 29:531–540

21. Goubergrits L, Affeld K (2004) Numerical estimation of blood damage in artificial organs. Artif Organs 28:499–507

22. Gu L, Smith WA (2005) Evaluation of computational models for hemolysis estimation. ASAIO journal 51:202–207

23. Arwatz G, Smits AJ (2013) A viscoelastic model of shear-induced hemolysis in laminar flow. Biorheology 50:45–55

24. Arora D (2006) Computational hemodynamics: Hemolysis and viscoelasticity. Rice University

25. Ezzeldin HM, de Tullio MD, Vanella M, Solares SD, Balaras E (2015) A strain-based model for mechanical hemolysis based on a coarse-grained red blood cell model. Ann Biomed Eng 43:1398–1409

26. Vitello DJ, Ripper RM, Fettiplace MR, Weinberg GL, Vitello JM (2015) Blood density is nearly equal to water density: a validation study of the gravimetric method of measuring intraoperative blood loss. J Vet Med 2015:

27. Chen Y, Sharp MK (2011) A strain-based flow-induced hemolysis prediction model calibrated by in vitro erythrocyte deformation measurements. Artif Organs 35:145–156

28. Dirkes N, Key F, Behr M (2024) Eulerian formulation of the tensor-based morphology equations for strain-based blood damage modeling. Comput Methods Appl Mech Eng 426:. https://doi.org/10.1016/j.cma.2024.116979

29. Rydquist G, Esmaily M (2022) A cell-resolved, Lagrangian solver for modeling red blood cell dynamics in macroscale flows. J Comput Phys 461:111204

30. Lo EW, Menezes LJ, Torii R (2020) On outflow boundary conditions for CT-based computation of FFR: Examination using PET images. Med Eng Phys 76:79–87. https://doi.org/10.1016/J.MEDENGPHY.2019.10.007

31. Lee HJ, Kim YW, Kim JH, Lee YJ, Moon J, Jeong P, Jeong J, Kim JS, Lee JS (2022) Optimization of FFR prediction algorithm for gray zone by hemodynamic features with synthetic model and biometric data. Comput Methods Programs Biomed 220:106827. https://doi.org/10.1016/J.CMPB.2022.106827

32. Zeng Y, Wang X, Tang Z, Li T, Jiang X, Ji F, Zhou Y, Ge J, Li Z, Zhao Y, Ma C, Mintz GS, Nie S (2023) Diagnostic accuracy of CT-FFR with a new coarse-to-fine subpixel algorithm in detecting lesion-specific ischemia: a prospective multicenter study. Revista Española de Cardiología (English Edition). https://doi.org/10.1016/j.rec.2023.05.008

33. Zhou B, Carrillo-Larco RM, Danaei G, Riley LM, Paciorek CJ, Stevens GA, Gregg EW, Bennett JE, Solomon B, Singleton RK, Sophiea MK, Iurilli MLC, Lhoste VPF, Cowan MJ, Savin S, Woodward M, Balanova Y, Cifkova R, Damasceno A, Elliott P, Farzadfar F, He J, Ikeda N, Kengne AP, Khang YH, Kim HC, Laxmaiah A, Lin HH, Maira PM, Miranda JJ, Neuhauser H, Sundström J, Varghese C, Widyahening IS, Zdrojewski T, Ezzati M, Abarca-Gómez L, Abdeen ZA, Abdul Rahim HF, Abu-Rmeileh NM, Acosta-Cazares B, Adams RJ, Aekplakorn W, Afsana K, Afzal S, Agdeppa IA, Aghazadeh-Attari J, Aguilar-Salinas CA, Agyemang C, Ahmad NA, Ahmadi A, Ahmadi N, Ahmadi N, Ahmadizar F, Ahmed SH, Ahrens W, Ajlouni K, Al-Raddadi R, Alarouj M, AlBuhairan F, AlDhukair S, Ali MM, Alkandari A, Alkerwi A, Allin K, Aly E, Amarapurkar DN, Amougou N, Amouyel P, Andersen LB, Anderssen SA, Anjana RM, Ansari-Moghaddam A, Ansong D, Aounallah-Skhiri H, Araújo J, Ariansen I, Aris T, Arku RE, Arlappa N, Aryal KK, Aspelund T, Assah FK, Assunção MCF, Auvinen J, Avdićová M, Azevedo A, Azimi-Nezhad M, Azizi F, Azmin M, Babu B V., Bahijri S, Balakrishna N, Bamoshmoosh M, Banach M, Banadinović M, Bandosz P, Banegas JR, Baran J, Barbagallo CM, Barceló A, Barkat A, Barreto M, Barros AJD, Barros MVG, Bartosiewicz A, Basit A, Bastos JLD, Bata I, Batieha AM, Batyrbek A, Baur LA, Beaglehole R, Belavendra A, Romdhane H Ben, Benet M, Benson LS, Berkinbayev S, Bernabe-Ortiz A, Bernotiene G, Bettiol H, Bezerra J, Bhagyalaxmi A, Bhargava SK, Bia D, Biasch K, Lele ECB, Bikbov MM, Bista B, Bjerregaard P, Bjertness E, Bjertness MB, Björkelund C, Bloch K V., Blokstra A, Bo S, Bobak M,

Boeing H, Boggia JG, Boissonnet CP, Bojesen SE, Bongard V, Bonilla-Vargas A, Braeckman L, Bruno G, Bueno-De-Mesquita HB, Burns C, Cardoso VC, Cervantes-Loaiza M, Chadjigeorgiou CA, Chamukuttan S, Chan AW, Chan Q, Chaturvedi HK, Chaturvedi N, Chee ML, Chen CJ, Chen F, Chen H, Chen S, Chen Z, Cheng CY, Cheraghian B, Dekkaki IC, Chetrit A, Chien KL, Chiolero A, Chiou ST, Chirita-Emandi A, Chirlaque MD, Cho B, Christensen K, Christofaro DG, Chudek J, Cinteza E, Claessens F, Clarke J, Clays E, Cohen E, Concin H, Cooper C, Coppinger TC, Costanzo S, Cottel D, Cowell C, Craig CL, Crampin AC, Crujeiras AB, Cruz JJ, Csilla S, Cui L, Cureau F V., Cuschieri S, D'Arrigo G, d'Orsi E, Dallongeville J, Dankner R, Dantoft TM, Dauchet L, Davletov K, De Backer G, De Bacquer D, De Curtis A, de Gaetano G, De Henauw S, de Oliveira PD, De Ridder D, De Smedt D, Deepa M, Deev AD, DeGennaro V, Delisle H, Demarest S, Dennison E, Deschamps V, Dhimal M, Di Castelnuovo AF, Dias-Da-Costa JS, Diaz A, Dickerson TT, Dika Z, Djalalinia S, Do HTP, Dobson AJ, Donfrancesco C, Donoso SP, Döring A, Dorobantu M, Dörr M, Doua K, Dragano N, Drygas W, Duante CA, Duboz P, Duda RB, Dulskiene V, Dushpanova A, Džakula A, Dzerve V, Dziankowska-Zaborszczyk E, Eddie R, Eftekhar E, Eggertsen R, Eghtesad S, Eiben G, Ekelund U, El-Khateeb M, El Ati J, Eldemire-Shearer D, Eliasen M, Elosua R, Erasmus RT, Erbel R, Erem C, Eriksen L, Eriksson JG, Escobedo-De la Peña J, Eslami S, Esmaeili A, Evans A, Faeh D, Fakhretdinova AA, Fall CH, Faramarzi E, Farjam M, Fattahi MR, Fawwad A, Felix-Redondo FJ, Felix SB, Ferguson TS, Fernandes RA, Fernández-Bergés D, Ferrante D, Ferrao T, Ferrari M, Ferrario MM, Ferreccio C, Ferreira HS, Ferrer E, Ferrieres J, Figueiró TH, Fink G, Fischer K, Foo LH, Forsner M, Fouad HM, Francis DK, do Carmo Franco M, Frikke-Schmidt R, Frontera G, Fuchs FD, Fuchs SC, Fujita Y, Fumihiko M, Furdela V, Furer A, Furusawa T, Gaciong Z, Galbarczyk A, Galenkamp H, Galvano F, Gao J, Gao P, Garcia-De-la-Hera M, Garcia P, Gareta D, Garnett SP, Gaspoz JM, Gasull M, Gazzinelli A, Gehring U, Geleijnse JM, George R, Ghanbari A, Ghasemi E, Gheorghe-Fronea OF, Ghimire A, Gialluisi A, Giampaoli S, Gieger C, Gill TK, Giovannelli J, Gironella G, Giwercman A, Gkiouras K, Goldberg M, Goldsmith RA, Gomez LF, Gomula A, Gonçalves Cordeiro da Silva B, Gonçalves H, Gonçalves M, Gonzalez-Chica DA, Gonzalez-Gross M, González-Rivas JP, González-Villalpando C, González-

Villalpando ME, Gonzalez AR, Gorbea MB, Gottrand F, Graff-Iversen S, Grafnetter D, Grajda A, Grammatikopoulou MG, Gregor RD, Grodzicki T, Grosso G, Gruden G, Gu D, Guan OP, Gudmundsson EF, Gudnason V, Guerrero R, Guessous I, Guimaraes AL, Gulliford MC, Gunnlaugsdottir J, Gunter MJ, Gupta PC, Gupta R, Gureje O, Gurzkowska B, Gutierrez L, Gutzwiller F, Ha S, Hadaegh F, Haghshenas R, Hakimi H, Halkjær J, Hambleton IR, Hamzeh B, Hange D, Hanif AAM, Hantunen S, Hao J, Hardman CM, Hari Kumar R, Hashemi-Shahri SM, Hata J, Haugsgjerd T, Hayes AJ, He Y, Heier M, Hendriks ME, Henrique RDS, Henriques A, Hernandez Cadena L, Herqutanto, Herrala S, Heshmat R, Hill AG, Ho SY, Ho SC, Hobbs M, Holdsworth M, Homayounfar R, Horasan Dinc G, Horimoto ARVR, Hormiga CM, Horta BL, Houti L, Howitt C, Htay TT, Htet AS, Htike MMT, Hu Y, Huerta JM, Huhtaniemi IT, Huiart L, Huisman M, Husseini AS, Huybrechts I, Hwalla N, Iacoviello L, Iannone AG, Ibrahim MM, Ibrahim Wong N, Ikram MA, Iotova V, Irazola VE, Ishida T, Isiguzo GC, Islam M, Islam SMS, Iwasaki M, Jackson RT, Jacobs JM, Jaddou HY, Jafar T, James K, Jamrozik K, Janszky I, Janus E, Jarvelin MR, Jasienska G, Jelaković A, Jelaković B, Jennings G, Jha AK, Jiang CQ, Jimenez RO, Jöckel KH, Joffres M, Johansson M, Jokelainen JJ, Jonas JB, Jørgensen T, Joshi P, Joukar F, Jóźwiak J, Juolevi A, Jurak G, Jureša V, Kaaks R, Kafatos A, Kajantie EO, Kalmatayeva Z, Kalpourtzi N, Kalter-Leibovici O, Kampmann FB, Kannan S, Karaglani E, Kårhus LL, Karki KB, Katibeh M, Katz J, Kauhanen J, Kaur P, Kavousi M, Kazakbaeva GM, Keil U, Boker LK, Keinänen-Kiukaanniemi S, Kelishadi R, Kemper HCG, Keramati M, Kerimkulova A, Kersting M, Key T, Khader YS, Khalili D, Khaw KT, Kheiri B, Kheradmand M, Khosravi A, Kiechl-Kohlendorfer U, Kiechl S, Killewo J, Kim DW, Kim J, Klakk H, Klimek M, Klumbiene J, Knoflach M, Kolle E, Kolsteren P, Kontto JP, Korpelainen R, Korrovits P, Kos J, Koskinen S, Kouda K, Kowlessur S, Koziel S, Kratenova J, Kriaucioniene V, Kristensen PL, Krokstad S, Kromhout D, Kruger HS, Kubinova R, Kuciene R, Kujala UM, Kulaga Z, Krishna Kumar R, Kurjata P, Kusuma YS, Kutsenko V, Kuulasmaa K, Kyobutungi C, Laatikainen T, Lachat C, Laid Y, Lam TH, Landrove O, Lanska V, Lappas G, Larijani B, Latt TS, Le Coroller G, Le Nguyen Bao K, Le TD, Lee J, Lee J, Lehmann N, Lehtimäki T, Lemogoum D, Levitt NS, Li Y, Lilly CL, Lim WY, Lima-Costa MF, Lin X, Lin YT, Lind L, Lingam V, Linneberg A,

Lissner L, Litwin M, Lo WC, Loit HM, Lopez-Garcia E, Lopez T, Lotufo PA, Lozano JE, Lovrenčić IL, Lukrafka JL, Luksiene D, Lundqvist A, Lundqvist R, Lunet N, Lustigová M, Luszczki E, Ma G, Ma J, Machado-Coelho GLL, Machado-Rodrigues AM, Macia E, Macieira LM, Madar AA, Maggi S, Magliano DJ, Magriplis E, Mahasampath G, Maire B, Majer M, Makdisse M, Malekzadeh F, Malekzadeh R, Malhotra R, Rao KM, Malyutina SK, Maniego L V., Manios Y, Mann JI, Mansour-Ghanaei F, Manzato E, Marcil A, Margozzini P, Mårild SB, Marinović Glavić M, Marques-Vidal P, Marques LP, Marrugat J, Martorell R, Mascarenhas LP, Matasin M, Mathiesen EB, Mathur P, Matijasevich A, Matlosz P, Matsha TE, Mavrogianni C, Mbanya JCN, Mc Donald Posso AJ, McFarlane SR, McGarvey ST, McLachlan S, McLean RM, McLean SB, McNulty BA, Mediene Benchekor S, Medzioniene J, Mehdipour P, Mehlig K, Mehrparvar AH, Meirhaeghe A, Meisinger C, Montano CM, Menezes AMB, Menon GR, Mereke A, Meshram II, Metspalu A, Meyer HE, Mi J, Michels N, Mikkel K, Milkowska K, Miller JC, Minderico CS, Mini GK, Mirjalili MR, Mirrakhimov E, Mišigoj-Duraković M, Modesti PA, Moghaddam SS, Mohajer B, Mohamed MK, Mohamed SF, Mohammad K, Mohammadi MR, Mohammadi Z, Mohammadifard N, Mohammadpourhodki R, Mohan V, Mohanna S, Mohd Yusoff MF, Mohebbi I, Mohebi F, Moitry M, Møllehave LT, Molnár D, Momenan A, Mondo CK, Monterrubio-Flores E, Monyeki KDK, Moon JS, Moosazadeh M, Moreira LB, Morejon A, Moreno LA, Morgan K, Moschonis G, Mossakowska M, Mostafa A, Mostafavi SA, Mota J, Motlagh ME, Motta J, Moura-Dos-Santos MA, Mridha MK, Msyamboza KP, Mu TT, Muhihi AJ, Muiesan ML, Müller-Nurasyid M, Murphy N, Mursu J, Musa KI, Milanović SM, Musil V, Mustafa N, Nabipour I, Naderimagham S, Nagel G, Naidu BM, Najafi F, Nakamura H, Námešná J, Nang EEK, Nangia VB, Narake S, Ndiaye NC, Neal WA, Nejatizadeh A, Nenko I, Neovius M, Nguyen CT, Nguyen ND, Nguyen Q V., Nguyen QN, Nieto-Martínez RE, Niiranen TJ, Nikitin YP, Ninomiya T, Nishtar S, Njelekela MA, Noale M, Noboa OA, Noorbala AA, Norat T, Nordendahl M, Nordestgaard BG, Noto D, Nowak-Szczepanska N, Nsour M Al, Nunes B, O'Neill TW, O'Reilly D, Ochimana C, Oda E, Odili AN, Oh K, Ohara K, Ohtsuka R, Olinto MTA, Oliveira IO, Omar MA, Onat A, Ong SK, Ono LM, Ordunez P, Ornelas R, Ortiz PJ, Osmond C, Ostojic SM, Ostovar A, Otero JA, Overvad K, Owusu-Dabo E, Paccaud FM,

Padez C, Pahomova E, de Paiva KM, Pająk A, Palli D, Palmieri L, Pan WH, Panda-Jonas S, Panza F, Paoli M, Papandreou D, Park SW, Park S, Parnell WR, Parsaeian M, Pasquet P, Patel ND, Pavlyshyn H, Pećin I, Pednekar MS, Pedro JM, Peer N, Peixoto SV, Peltonen M, Pereira AC, Peres KGDA, Peres MA, Peters A, Petkeviciene J, Peykari N, Pham ST, Pichardo RN, Pigeot I, Pikhart H, Pilav A, Pilotto L, Pitakaka F, Piwonska A, Pizarro A, Pedro Plans-Rubió, Polašek O, Porta M, Poudyal A, Pourfarzi F, Pourshams A, Poustchi H, Pradeepa R, Price AJ, Price JF, Providencia R, Puhakka SE, Puiu M, Punab M, Qasrawi RF, Qorbani M, Queiroz D, Quoc Bao T, Radić I, Radisauskas R, Rahimikazerooni S, Rahman M, Raitakari O, Raj M, Rakhimova EM, Rao SR, Ramachandran A, Ramos E, Rampal L, Rampal S, Rangel Reina DA, Rarra V, Ricardo Rech C, Redon J, Reganit PFM, Regecová V, Revilla L, Rezaianzadeh A, Ribeiro R, Riboli E, Richter A, Rigo F, Rinke de Wit TF, Ritti-Dias RM, Robitaille C, Rodríguez-Artalejo F, Rodriguez-Perez MDC, Rodríguez-Villamizar LA, Roggenbuck U, Rojas-Martinez R, Romaguera D, Romeo EL, Rosengren A, Roy JGR, Rubinstein A, Ruidavets JB, Ruiz-Betancourt BS, Ruiz-Castell M, Rusakova IA, Russo P, Rutkowski M, Sabanayagam C, Sabbaghi H, Sachdev HS, Sadjadi A, Safarpour AR, Safi S, Safiri S, Saidi O, Sakarya S, Saki N, Salanave B, Salazar Martinez E, Salmerón D, Salomaa V, Salonen JT, Salvetti M, Sánchez-Abanto J, Sans S, Santos DA, Santos IS, Santos LC, Santos MP, Santos R, Saramies JL, Sardinha LB, Sarganas G, Sarrafzadegan N, Sathish T, Saum KU, Savva S, Sawada N, Sbaraini M, Scazufca M, Schaan BD, Schargrodsky H, Schipf S, Schmidt CO, Schnohr P, Schöttker B, Schramm S, Schultsz C, Schutte AE, Sebert S, Sein AA, Sen A, Senbanjo IO, Sepanlou SG, Servais J, Shalnova SA, Shamah-Levy T, Shamshirgaran M, Shanthirani CS, Sharafkhah M, Sharma SK, Shaw JE, Shayanrad A, Shayesteh AA, Shi Z, Shibuya K, Shimizu-Furusawa H, Shin DW, Shirani M, Shiri R, Shrestha N, Si-Ramlee K, Siani A, Siantar R, Sibai AM, Silva CRDM, Santos Silva DA, Simon M, Simons J, Simons LA, Sjöström M, Slowikowska-Hilczer J, Slusarczyk P, Smeeth L, So HK, Soares FC, Sobngwi E, Söderberg S, Soemantri A, Sofat R, Solfrizzi V, Somi MH, Sonestedt E, Song Y, Sørensen TIA, Sørgjerd EP, Sorić M, Sossa Jérome C, Soumaré A, Sparboe-Nilsen B, Sparrenberger K, Staessen JA, Starc G, Stavreski B, Steene-Johannessen J, Stehle P, Stein AD, Stergiou GS, Stessman J, Stieber J, Stöckl D, Stocks T, Stokwiszewski J, Stronks K,

Strufaldi MW, Suka M, Sun CA, Sung YT, Suriyawongpaisal P, Sy RG, Syddall HE, Sylva RC, Szklo M, Shyong Tai E, Tammesoo ML, Tamosiunas A, Tan EJ, Tang X, Tanser F, Tao Y, Tarawneh MR, Tarqui-Mamani CB, Taylor A, Taylor J, Tebar WR, Tell GS, Tello T, Tham YC, Thankappan KR, Theobald H, Theodoridis X, Thijs L, Thinggaard M, Thomas N, Thorand B, Thuesen BH, Timmermans EJ, Tjandrarini DH, Tjonneland A, Toft U, Tolonen HK, Tolstrup JS, Topbas M, Topór-Madry R, Tormo MJ, Tornaritis MJ, Torrent M, Torres-Collado L, Touloumi G, Traissac P, Triantafyllou A, Trichopoulos D, Trichopoulou A, Trinh OTH, Trivedi A, Tshepo L, Tsugane S, Tuliakova AM, Tulloch-Reid MK, Tullu F, Tuomainen TP, Tuomilehto J, Turley ML, Twig G, Tynelius P, Tzourio C, Ueda P, Ugel E, Ulmer H, Uusitalo HMT, Valdivia G, Valvi D, van Dam RM, van den Born BJ, Van der Heyden J, van der Schouw YT, Van Herck K, Van Minh H, Van Schoor NM, van Valkengoed IGM, van Zutphen EM, Vanderschueren D, Vanuzzo D, Varbo A, Vasan SK, Vega T, Veidebaum T, Velasquez-Melendez G, Veronesi G, Verschuren WMM, Verstraeten R, Victora CG, Viet L, Villalpando S, Vineis P, Vioque J, Virtanen JK, Visvikis-Siest S, Viswanathan B, Vlasoff T, Vollenweider P, Voutilainen A, Wade AN, Walton J, Wambiya EOA, Wan Bebakar WM, Wan Mohamud WN, Wanderley RDS, Wang MD, Wang N, Wang Q, Wang X, Wang YX, Wang YW, Wannamethee SG, Wareham N, Wei W, Weres A, Werner B, Whincup PH, Widhalm K, Wiecek A, Wilks RJ, Willeit J, Willeit P, Williams EA, Wilsgaard T, Wojtyniak B, Wong-McClure RA, Wong A, Wong TY, Woo J, Wu FC, Wu S, Wyszynska J, Xu H, Xu L, Yaacob NA, Yan W, Yang L, Yang X, Yang Y, Yasuharu T, Ye X, Yiallouros PK, Yoosefi M, Yoshihara A, You SL, Younger-Coleman NO, Yusoff AF, Zainuddin AA, Zakavi SR, Zamani F, Zambon S, Zampelas A, Zapata ME, Zaw KK, Zejglicova K, Zeljkovic Vrkic T, Zeng Y, Zhang L, Zhang ZY, Zhao D, Zhao MH, Zhen S, Zheng Y, Zholdin B, Zhu D, Zins M, Zitt E, Zocalo Y, Zoghlami N, Zuñiga Cisneros J (2021) Worldwide trends in hypertension prevalence and progress in treatment and control from 1990 to 2019: a pooled analysis of 1201 population-representative studies with 104 million participants. The Lancet 398:957–980. https://doi.org/10.1016/S0140-6736(21)01330-1

34. Dukát A, Kolesár J, Gavornik P, Mikeš Z, Zvonár J (1989) Longterm follow-up of hypertensive patients with holter ECG and blood pressure monitorings. International Journal of Psychophysiology 7:188–190. https://doi.org/10.1016/0167-8760(89)90136-0

35. Schulz RA, Stein JA, Pelc NJ (2021) How CT happened: the early development of medical computed tomography. Journal of Medical Imaging 8:. https://doi.org/10.1117/1.jmi.8.5.052110

36. Bouma BE, Tearney GJ, Yabushita H, Shishkov M, Kauffman CR, DeJoseph Gauthier D, MacNeill BD, Houser SL, Aretz HT, Halpern EF, Jang IK (2003) Evaluation of intracoronary stenting by intravascular optical coherence tomography. Heart 89:317–320. https://doi.org/10.1136/heart.89.3.317

37. Jang I-K, Bouma BE, Kang D-H, Park S-J, Park S-W, Seung K-B, Choi K-B, Shishkov M, Schlendorf K, Pomerantsev E, Houser SL, Thomas Aretz H, Tearney GJ (2002) Visualization of Coronary Atherosclerotic Plaques in Patients Using Optical Coherence Tomography: Comparison With Intravascular Ultrasound

38. Dohad S, Zhu A, Krishnan S, Wang F, Wang S, Cox J, Henry TD (2018) Optical coherence tomography guided carotid artery stent procedure: technique and potential applications. Catheterization and Cardiovascular Interventions 91:521–530. https://doi.org/10.1002/ccd.27344

39. Schwindt AG, Bennett JG, Crowder WH, Dohad S, Janzer SF, George JC, Tedder B, Davis TP, Cawich IM, Gammon RS, Muck PE, Pigott JP, Dishmon DA, Lopez LA, Golzar JA, Chamberlin JR, Moulton MJ, Zakir RM, Kaki AK, Fishbein GJ, McDaniel HB, Hezi-Yamit A, Simpson JB, Desai A (2017) Lower Extremity Revascularization Using Optical Coherence Tomography-Guided Directional Atherectomy: Final Results of the EValuation of the PantheriS Optical COherence Tomography ImagiNg Atherectomy System for Use in the Peripheral Vasculature (VISION) Study. Journal of Endovascular Therapy 24:355–366. https://doi.org/10.1177/1526602817701720

40. Araki M, Park SJ, Dauerman HL, Uemura S, Kim JS, Di Mario C, Johnson TW, Guagliumi G, Kastrati A, Joner M, Holm NR, Alfonso F, Wijns W, Adriaenssens T, Nef H, Rioufol G, Amabile N, Souteyrand G, Meneveau N,

Gerbaud E, Opolski MP, Gonzalo N, Tearney GJ, Bouma B, Aguirre AD, Mintz GS, Stone GW, Bourantas C V., Räber L, Gili S, Mizuno K, Kimura S, Shinke T, Hong MK, Jang Y, Cho JM, Yan BP, Porto I, Niccoli G, Montone RA, Thondapu V, Papafaklis MI, Michalis LK, Reynolds H, Saw J, Libby P, Weisz G, Iannaccone M, Gori T, Toutouzas K, Yonetsu T, Minami Y, Takano M, Raffel OC, Kurihara O, Soeda T, Sugiyama T, Kim HO, Lee T, Higuma T, Nakajima A, Yamamoto E, Bryniarski KL, Di Vito L, Vergallo R, Fracassi F, Russo M, Seegers LM, McNulty I, Park S, Feldman M, Escaned J, Prati F, Arbustini E, Pinto FJ, Waksman R, Garcia-Garcia HM, Maehara A, Ali Z, Finn A V., Virmani R, Kini AS, Daemen J, Kume T, Hibi K, Tanaka A, Akasaka T, Kubo T, Yasuda S, Croce K, Granada JF, Lerman A, Prasad A, Regar E, Saito Y, Sankardas MA, Subban V, Weissman NJ, Chen Y, Yu B, Nicholls SJ, Barlis P, West NEJ, Arbab-Zadeh A, Ye JC, Dijkstra J, Lee H, Narula J, Crea F, Nakamura S, Kakuta T, Fujimoto J, Fuster V, Jang IK (2022) Optical coherence tomography in coronary atherosclerosis assessment and intervention. Nat Rev Cardiol 19:684–703

41. Waxman S, Dixon SR, L'Allier P, Moses JW, Petersen JL, Cutlip D, Tardif JC, Nesto RW, Muller JE, Hendricks MJ, Sum ST, Gardner CM, Goldstein JA, Stone GW, Krucoff MW (2009) In Vivo Validation of a Catheter-Based Near-Infrared Spectroscopy System for Detection of Lipid Core Coronary Plaques. Initial Results of the SPECTACL Study. JACC Cardiovasc Imaging 2:858–868. https://doi.org/10.1016/j.jcmg.2009.05.001

42. Finn A V., Kolodgie FD, Virmani R (2010) Correlation between carotid intimal/medial thickness and atherosclerosis: A point of view from pathology. Arterioscler Thromb Vasc Biol 30:177–181

43. Lal BK, Hobson RW, Pappas PJ, Kubicka R, Hameed M, Chakhtura EY, Jamil Z, Padberg FT, Haser PB, Durán WN (2002) Pixel distribution analysis of B-mode ultrasound scan images predicts histologic features of atherosclerotic carotid plaques. J Vasc Surg 35:1210–1217. https://doi.org/10.1067/mva.2002.122888

44. Noflatscher M, Hunjadi M, Schreinlechner M, Sommer P, Lener D, Theurl M, Kirchmair R, Bauer A, Ritsch A, Marschang P (2023) Inverse Correlation of

Cholesterol Efflux Capacity with Peripheral Plaque Volume Measured by 3D Ultrasound. Biomedicines 11:1918. https://doi.org/10.3390/biomedicines11071918

45. Hegner A, Wittek A, Derwich W, Huß A, Gámez AJ, Blase C (2023) Using averaged models from 4D ultrasound strain imaging allows to significantly differentiate local wall strains in calcified regions of abdominal aortic aneurysms. Biomech Model Mechanobiol. https://doi.org/10.1007/s10237-023-01738-x

46. Moneta GL, Edwards JM, Chitwood RW, Taylor LM, Lee RW, Cummings CA, Porter JM (1993) Correlation of North American Symptomatic Carotid Endarterectomy Trial (NASCET) angiographic definition of 70% to 99% internal carotid artery stenosis with duplex scanning. J Vasc Surg 17:152–159. https://doi.org/10.1016/0741-5214(93)90019-I

47. Josephson SA, Bryant SO, Mak HK, Johnston SC, Dillon WP, Smith WS (2004) Evaluation of carotid stenosis using CT angiography in the initial evaluation of stroke and TIA. Neurology 63:457. https://doi.org/10.1212/01.WNL.0000135154.53953.2C

48. Maurovich-Horvat P, Ferencik M, Voros S, Merkely B, Hoffmann U (2014) Comprehensive plaque assessment by coronary CT angiography. Nat Rev Cardiol 11:390–402. https://doi.org/10.1038/nrcardio.2014.60

49. Divakaran S, Cheezum MK, Hulten EA, Bittencourt MS, Silverman MG, Nasir K, Blankstein R (2015) Use of cardiac CT and calcium scoring for detecting coronary plaque: Implications on prognosis and patient management. British Journal of Radiology 88

50. Motoyama S, Ito H, Sarai M, Kondo T, Kawai H, Nagahara Y, Harigaya H, Kan S, Anno H, Takahashi H, Naruse H, Ishii J, Hecht H, Shaw LJ, Ozaki Y, Narula J (2015) Plaque Characterization by Coronary Computed Tomography Angiography and the Likelihood of Acute Coronary Events in Mid-Term Follow-Up. J Am Coll Cardiol 66:337–346. https://doi.org/10.1016/J.JACC.2015.05.069

51. Maurovich-Horvat P, Hoffmann U, Vorpahl M, Nakano M, Virmani R, Alkadhi H (2010) The Napkin-Ring Sign: CT Signature of High-Risk Coronary Plaques?

JACC Cardiovasc Imaging 3:440–444. https://doi.org/10.1016/J.JCMG.2010.02.003

52. Dweck MR, Williams MC, Moss AJ, Newby DE, Fayad ZA (2016) Computed Tomography and Cardiac Magnetic Resonance in Ischemic Heart Disease. J Am Coll Cardiol 68:2201–2216. https://doi.org/10.1016/J.JACC.2016.08.047

53. Akçakaya M, Basha TA, Chan RH, Manning WJ, Nezafat R (2014) Accelerated isotropic sub-millimeter whole-heart coronary MRI: Compressed sensing versus parallel imaging. Magn Reson Med 71:815–822. https://doi.org/10.1002/mrm.24683

54. Ong WY, Im K, Anias EGD, Atthias M, Tuber S, Lamm CDF, Ven S, Lein P, Agel IN, Usan S, Angerak EL, Liver O, Eber MW, Edersen RMP, Chmidt S, Otnar EMB, Arren W, Anning JM (2001) CORONARY MAGNETIC RESONANCE ANGIOGRAPHY FOR THE DETECTION OF CORONARY STENOSES

55. Hatsukami TS, Ross R, Polissar NL, Yuan C (2000) Visualization of Fibrous Cap Thickness and Rupture in Human Atherosclerotic Carotid Plaque In Vivo With High-Resolution Magnetic Resonance Imaging

56. Kerwin WS, Zhao X, Chun Y, Hatsukami TS, Maravilla KR, Underhill HR, Zhao X (2009) Contrast-enhanced MRI of carotid atherosclerosis: Dependence on contrast agent. Journal of Magnetic Resonance Imaging 30:35–40. https://doi.org/10.1002/jmri.21826

57. Zhang J, Rothenberger SM, Brindise MC, Markl M, Rayz VL, Vlachos PP (2022) Wall Shear Stress Estimation for 4D Flow MRI Using Navier–Stokes Equation Correction. Ann Biomed Eng 50:1810–1825. https://doi.org/10.1007/s10439-022-02993-2

58. Nath R, Kazemi A, Callahan S, Stoddard MF, Amini AA (2023) 4Dflow-VP-Net: A deep convolutional neural network for noninvasive estimation of relative pressures in stenotic flows from 4D flow MRI. Magn Reson Med. https://doi.org/10.1002/mrm.29791

59. Shahid L, Rice J, Berhane H, Rigsby C, Robinson J, Griffin L, Markl M, Roldán-Alzate A (2022) Enhanced 4D Flow MRI-Based CFD with Adaptive

Mesh Refinement for Flow Dynamics Assessment in Coarctation of the Aorta. Ann Biomed Eng 50:1001–1016. https://doi.org/10.1007/s10439-022-02980-7

60. Sotelo J, Mura J, Hurtado D, Uribe S (2019) A novel MATLAB toolbox for processing 4D Flow MRI data. International Society of Magnetic Reso-nance in Medicine (ISMRM)

61. Vali A, Aristova M, Vakil P, Abdalla R, Prabhakaran S, Markl M, Ansari SA, Schnell S (2019) Semi-automated analysis of 4D flow MRI to assess the hemodynamic impact of intracranial atherosclerotic disease. Magn Reson Med 82:749–762. https://doi.org/10.1002/mrm.27747

62. Zhuang B, Sirajuddin A, Zhao S, Lu M (2021) The role of 4D flow MRI for clinical applications in cardiovascular disease: Current status and future perspectives. Quant Imaging Med Surg 11:4193–4210

63. Ramaekers MJFG, Westenberg JJM, Adriaans BP, Nijssen EC, Wildberger JE, Lamb HJ, Schalla S (2023) A clinician's guide to understanding aortic 4D flow MRI. Insights Imaging 14

64. Malec E, Schmidt C, Lehner A, Januszewska K (2017) Results of the Fontan operation with no early mortality in 248 consecutive patients. Kardiol Pol 75:255–260. https://doi.org/10.5603/KP.a2016.0170

65. ANSYS I (2015) ANSYS fluent UDF manual. ANSYS, Inc, Canonsburg, PA

66. Marchisio DL, Fox RO (2005) Solution of population balance equations using the direct quadrature method of moments. J Aerosol Sci 36:43–73

67. Shi Y, Lawford P, Hose R (2011) Review of Zero-D and 1-D Models of Blood Flow in the Cardiovascular System. Biomed Eng Online 10

68. Kim HJ, Vignon-Clementel IE, Coogan JS, Figueroa CA, Jansen KE, Taylor CA (2010) Patient-specific modeling of blood flow and pressure in human coronary arteries. Ann Biomed Eng 38:3195–3209. https://doi.org/10.1007/s10439-010-0083-6

69. Parker LP, Svensson Marcial A, Brismar TB, Broman LM, Prahl Wittberg L (2024) In silico parametric analysis of femoro-jugular venovenous ECMO and return cannula dynamics: In silico analysis of femoro-jugular VV ECMO. Med Eng Phys 125:. https://doi.org/10.1016/j.medengphy.2024.104126

70. Carbonaro D, Villa E, Gallo D, Morbiducci U, Audenino AL, Chiastra C (2024) Designing the mechanical behavior of NiTi self-expandable vascular stents by tuning the heat treatment parameters. J Mech Behav Biomed Mater 106653. https://doi.org/10.1016/j.jmbbm.2024.106653

71. Antonowicz A, Wojtas K, Makowski Ł, Orciuch W, Kozłowski M (2023) Particle Image Velocimetry of 3D-Printed Anatomical Blood Vascular Models Affected by Atherosclerosis. Materials 16:1055. https://doi.org/10.3390/ma16031055

72. Jędrzejczak K, Antonowicz A, Makowski Ł, Orciuch W, Wojtas K, Kozłowski M (2023) Computational Fluid Dynamics validated by micro Particle Image Velocimetry to estimate the risk of hemolysis in arteries with atherosclerotic lesions. Chemical Engineering Research and Design. https://doi.org/10.1016/j.cherd.2023.06.041

73. Vergine F, Maddalena L (2014) Stereoscopic particle image velocimetry measurements of supersonic, turbulent, and interacting streamwise vortices: challenges and application. Progress in Aerospace Sciences 66:1–16. https://doi.org/10.1016/J.PAEROSCI.2013.12.001

74. Saaid H, Voorneveld J, Schinkel C, Westenberg J, Gijsen F, Segers P, Verdonck P, de Jong N, Bosch JG, Kenjeres S, Claessens T (2019) Tomographic PIV in a model of the left ventricle: 3D flow past biological and mechanical heart valves. J Biomech 90:40–49. https://doi.org/10.1016/J.JBIOMECH.2019.04.024

75. DeMarchi N, White C (2012) Echo particle image velocimetry. J Vis Exp. https://doi.org/10.3791/4265

76. Voorneveld J, Saaid H, Schinkel C, Radeljic N, Lippe B, Gijsen FJH, van der Steen AFW, de Jong N, Claessens T, Vos HJ, Kenjeres S, Bosch JG (2020) 4-D Echo-Particle Image Velocimetry in a Left Ventricular Phantom. Ultrasound Med Biol 46:805–817. https://doi.org/10.1016/J.ULTRASMEDBIO.2019.11.020

77. Caridi GCA, Torta E, Mazzi V, Chiastra C, Audenino AL, Morbiducci U, Gallo D (2022) Smartphone-based particle image velocimetry for cardiovascular flows applications: A focus on coronary arteries. Front Bioeng Biotechnol 10:. https://doi.org/10.3389/fbioe.2022.1011806

78. Park H, Yeom E, Lee SJ (2016) X-ray PIV measurement of blood flow in deep vessels of a rat: An in vivo feasibility study. Sci Rep 6:. https://doi.org/10.1038/srep19194

79. Illi J, Bernhard B, Nguyen C, Pilgrim T, Praz F, Gloeckler M, Windecker S, Haeberlin A, Gräni C (2022) Translating Imaging Into 3D Printed Cardiovascular Phantoms: A Systematic Review of Applications, Technologies, and Validation. JACC Basic Transl Sci 7:1050–1062. https://doi.org/10.1016/J.JACBTS.2022.01.002

80. Jędrzejek M, Peszek-Przybyła E, Jadczyk T, Zemik J, Piprek P, Pysz P, Kozłowski M, Wojakowski W, Smolka G (2023) 3D printing from transesophageal echocardiography for planning mitral paravalvular leak closure - feasibility study. Postepy w Kardiologii Interwencyjnej 19:270–276. https://doi.org/10.5114/aic.2023.131481

81. Irnstorfer N, Unger E, Hojreh A, Homolka P (2019) An anthropomorphic phantom representing a prematurely born neonate for digital x-ray imaging using 3D printing: Proof of concept and comparison of image quality from different systems. Sci Rep 9:. https://doi.org/10.1038/s41598-019-50925-3

82. Otton JM, Birbara NS, Hussain T, Greil G, Foley TA, Pather N (2017) 3D printing from cardiovascular CT: A practical guide and review. Cardiovasc Diagn Ther 7:507–526

83. Castro-Sastre MÁ, Fernández-Abia AI, Piep J, Rodríguez-González P, Barreiro J (2020) Towards functional parts by binder jetting calcium-sulphate with thermal treatment post-processing. Materials 13:. https://doi.org/10.3390/ma13173818

84. Salmi M (2021) Additive manufacturing processes in medical applications. Materials 14:1–16

85. Bałdyga J, Orciuch W, Makowski Ł, Malski-Brodzicki M, Malik K (2008) Break-Up of Nanoparticle Clusters—Process Modeling. J Dispers Sci Technol 29:555–563

86. Bałdyga J, Orciuch W, Makowski Ł, Krasiński A, Malski-Brodzicki M, Malik K (2008) Shear Flow of Aggregated Nanosuspensions–Fundamentals and Model Formulation. J Dispers Sci Technol 29:564–572

87. Bałdyga J, Orciuch W, Makowski Ł, Malik K, Özcan-Taşkin G, Eagles W, Padron G (2008) Dispersion of nanoparticle clusters in a rotor- stator mixer. Ind Eng Chem Res 47:3652–3663

88. Jędrzejczak K, Makowski Ł, Orciuch W (2023) Model of blood rheology including hemolysis based on population balance. Commun Nonlinear Sci Numer Simul 116:106802. https://doi.org/10.1016/J.CNSNS.2022.106802

89. Razavi A, Shirani E, Sadeghi MR (2011) Numerical simulation of blood pulsatile flow in a stenosed carotid artery using different rheological models. J Biomech 44:2021–2030. https://doi.org/10.1016/j.jbiomech.2011.04.023

90. Boyd J, Buick JM, Green S (2007) Analysis of the Casson and Carreau-Yasuda non-Newtonian blood models in steady and oscillatory flows using the lattice Boltzmann method. Physics of Fluids 19:93103

91. Shibeshi SS, Collins WE (2005) The rheology of blood flow in a branched arterial system. Applied Rheology 15:398–405

92. Morbiducci U, Gallo D, Massai D, Ponzini R, Deriu MA, Antiga L, Redaelli A, Montevecchi FM (2011) On the importance of blood rheology for bulk flow in hemodynamic models of the carotid bifurcation. J Biomech 44:2427–2438. https://doi.org/https://doi.org/10.1016/j.jbiomech.2011.06.028

93. Chien S (1970) Shear dependence of effective cell volume as a determinant of blood viscosity. Science (1979) 168:977–979

94. Brooks DE, Goodwin JW, Seaman G V (1970) Interactions among erythrocytes under shear. J Appl Physiol 28:172–177

95. Zydney AL, Oliver III JD, Colton CK (1991) A constitutive equation for the viscosity of stored red cell suspensions: Effect of hematocrit, shear rate, and suspending phase. J Rheol (N Y N Y) 35:1639–1680

96. Giannokostas K, Moschopoulos P, Varchanis S, Dimakopoulos Y, Tsamopoulos J (2020) Advanced constitutive modeling of the thixotropic elasto-visco-plastic

behavior of blood: Description of the model and rheological predictions. Materials 13:4184

97. Jariwala S, Horner JS, Wagner NJ, Beris AN (2020) Application of population balance-based thixotropic model to human blood. J Nonnewton Fluid Mech 281:104294

98. Owens RG (2006) A new microstructure-based constitutive model for human blood. J Nonnewton Fluid Mech 140:57–70

99. Moyers-Gonzalez M, Owens RG, Fang J (2008) A non-homogeneous constitutive model for human blood. Part 1. Model derivation and steady flow. J Fluid Mech 617:327–354

100. Moyers-Gonzalez MA, Owens RG (2008) A non-homogeneous constitutive model for human blood: Part II. Asymptotic solution for large Péclet numbers. J Nonnewton Fluid Mech 155:146–160

101. Moyers-Gonzalez MA, Owens RG, Fang J (2008) A non-homogeneous constitutive model for human blood: Part III. Oscillatory flow. J Nonnewton Fluid Mech 155:161–173

102. Alemu Y, Bluestein D (2007) Flow-induced platelet activation and damage accumulation in a mechanical heart valve: numerical studies. Artif Organs 31:677–688

103. Fraser KH, Zhang T, Taskin ME, Griffith BP, Wu ZJ (2012) A quantitative comparison of mechanical blood damage parameters in rotary ventricular assist devices: shear stress, exposure time and hemolysis index. J Biomech Eng 134:

104. Puentener P, Schuck M, Kolar JW (2020) CFD Assisted Evaluation of in Vitro Experiments on Bearingless Blood Pumps. IEEE Trans Biomed Eng

105. Wiegmann L, Boës S, de Zélicourt D, Thamsen B, Daners MS, Meboldt M, Kurtcuoglu V (2018) Blood pump design variations and their influence on hydraulic performance and indicators of hemocompatibility. Ann Biomed Eng 46:417–428

106. Zhao TY, Xu GQ, Xue JY, Cai DY, Yang BW, Ba YY, Feng CY, Li TX, Gao BL, Chen ZC (2024) Effects of percutaneous endovascular angioplasty for

severe stenosis or occlusion of subclavian artery. Sci Rep 14:. https://doi.org/10.1038/s41598-024-65302-y

107. Buccheri D, Piraino D, Andolina G, Cortese B (2016) Understanding and managing in-stent restenosis: A review of clinical data, from pathogenesis to treatment. J Thorac Dis 8:E1150–E1162

108. Mhaimeed O, Burney ZA, Schott SL, Kohli P, Marvel FA, Martin SS (2024) The importance of LDL-C lowering in atherosclerotic cardiovascular disease prevention: Lower for longer is better. Am J Prev Cardiol 18:100649. https://doi.org/10.1016/J.AJPC.2024.100649

109. Mie B, Shoaib A, George DS, Anette V, Anne L, R KP, G NB (2023) Elevated LDL Triglycerides and Atherosclerotic Risk. J Am Coll Cardiol 81:136–152. https://doi.org/10.1016/j.jacc.2022.10.019

110. Wang HH, Garruti G, Liu M, Portincasa P, Wang DQH (2017) Cholesterol and Lipoprotein Metabolism and Atherosclerosis: Recent Advances in Reverse Cholesterol Transport. Ann Hepatol 16:S27–S42. https://doi.org/10.5604/01.3001.0010.5495

111. Sanin V, Schmieder RS, Koenig W (2024) Early action, lifelong impact: the crucial role of early detection, risk stratification, and aggressive treatment of familial hypercholesterolaemia. Eur J Prev Cardiol 31:889–891

112. Kimura T, Abe K, Shizuta S, Odashiro K, Yoshida Y, Sakai K, Kaitani K, Inoue K, Nakagawa Y, Yokoi H, Iwabuchi M, Hamasaki N, Nosaka H, Nobuyoshi M (2002) Long-term clinical and angiographic follow-up after coronary stent placement in native coronary arteries. Circulation 105:2986–2991. https://doi.org/10.1161/01.CIR.0000019743.11941.3B

113. Stevens JR, Zamani A, Osborne JIA, Zamani R, Akrami M (2021) Critical evaluation of stents in coronary angioplasty: a systematic review. Biomed Eng Online 20

114. Huo R, Liu Y, Xu H, Li J, Xin R, Xing Z, Deng S, Wang T, Yuan H, Zhao X (2022) Associations between carotid atherosclerotic plaque characteristics determined by magnetic resonance imaging and improvement of cognition in

patients undergoing carotid endarterectomy. Quant Imaging Med Surg 12:2891–2903. https://doi.org/10.21037/qims-21-981

115. Leader JH, Kanji R, Gorog DA (2024) Spontaneous reperfusion in STEMI: Its mechanisms and possible modulation. Kardiol Pol 82:363–374

116. Xodo A, Gregio A, Pilon F, Milite D, Danesi TH, Badalamenti G, Lepidi S, D'Oria M (2024) Carotid Interventions in Patients Undergoing Coronary Artery Bypass Grafting: A Narrative Review. J Clin Med 13